2-D MATHEMATICAL MODELLING OF HYDROGEN STORAGE IN METAL HYDRIDES

by

Gülşad Küçük

B.S., M.E., Boğaziçi University, 2006

Submitted to the Institute for Graduate Studies in
Science and Engineering in partial fulfillment of
the requirements for the degree of
Master of Science

Graduate Program in Mechanical Engineering
Boğaziçi University
2009

2-D MATHEMATICAL MODELLING OF HYDROGEN STORAGE IN METAL HYDRIDES

APPROVED BY:

Assist. Prof. Emre Aksan   . . . .
(Thesis Supervisor)

Assoc. Prof. Hasan Bedir   . . . .

Prof. Erhan Aksoylu   . . . .

Assist. Prof. Murat Çelik   . . . .

Assist. Prof. Hakan Ertürk   . . . .

DATE OF APPROVAL: 04.06.2009

To my lovely grandmother ,

"Sultan of Sultans",

Nimet Ersavaş

ACKNOWLEDGEMENTS

I would like to express sincere gratitude to my thesis supervisor Assist. Prof. Emre Aksan for his guidance and endless goodwill during my study.

I would like to thank Assoc. Prof. Hasan Bedir for his support and willingness to help me any time when I was in need.

I am also grateful to Erhan Turan for his invaluable help, patience and constant guidance.

Special thanks and appreciation go to my parents, my aunt Zeynep Zümrüt Bakır for their endless support and love.

Finally, I would like to express my best feelings to all of my friends who were beside me.

ABSTRACT

2-D MATHEMATICAL MODELLING OF HYDROGEN STORAGE IN METAL HYDRIDES

In this study a numerical model which simulates heat and mass transfer processes of hydrogen absorption in $LaNi_5$ is studied. Energy balance method is used for discretizing the heat equation. Transient heat conduction with convective boundary conditions is evaluated with explicit scheme. The analyses are conducted using MATLAB. Evaluation of temperature profiles and hydrogen mass that is being absorbed during hydriding are shown to be correlated with the experimental data and with the previous numerical studies.

Since the hydriding reaction is exothermic, the rate of removal of heat released is critical in time needed to reach saturation in metal-hydride reactor. The effects of bed geometry, inlet hydrogen pressure, and metal porosity, initial bed temperature and the temperature of cooling fluid are investigated. Different cases are compared with the base case which is chosen to have similarities with conventional metal hydride tanks in reactor geometry and in thermophysical properties.

ÖZET

METAL HİDRİTLERDE HİDROJEN DEPOLANMASININ 2 BOYUTTA MATEMATİKSEL MODELLENMESİ

Bu çalışmada $LaNi_5$'de hidrojen emilimi sırasındaki ısı ve kütle transferini simule eden bir nümerik model oluşturulmuştur. Isı denkleminin ayrık ifadesinde enerji denge metodu uygulanmıştır. Geçici ısı taşınımı, konvektif sınır koşulları altında değerlendirilmiştir. Analizler MATLAB kullanılarak tamamlanmıştır. Elde edilen sıcaklık profillerinin ve absorbe edilen hidrojen kütle değerlerinin literatürde belirtilen deney verileri ve önceki çalışmalarla uygunluk sağladığı görülmüştür.

Hidritleşme reaksiyonu egzotermik olduğundan, açığa çıkan ısının ortamdan uzaklaştırılması metal alışımın doygunluğa ulaşması için gerekli süre açısından çok önemlidir. Konvansiyonel hidrojen tüplerinin özellileri esas alınarak yapılan simulasyonlarda reaktör geometrisinin, içeri basılan hidrojenin basıncının, metalin gözeneklilik değerinin, metal yatağının ilk sıcaklığının ve soğutma amaçlı kullanılan akışkanın sıcaklığının; hidritleşme süresi ve miktar üzerine olan etkileri incelenmiştir.

TABLE OF CONTENTS

LIST OF FIGURES

LIST OF TABLES

LIST OF SYMBOLS/ABBREVIATIONS

C_a	Absorption constant
C_d	Desorption constant
C_p	Specific heat
C_{pg}	Specific heat for gaseous phase
C_{ps}	Specific heat for solid phase
E_a	Absorption activation energy
E_d	Desorption activation energy
h	Heat transfer coefficient
H	Height of reactor
H/M	Hydrogen to metal atomic ratio
h_{gs}	Heat transfer coefficient between solid and gas
k	Thermal conductivity
k_e	Effective thermal conductivity for metal-hydride bed
k_{ge}	Effective thermal conductivity for gaseous phase
k_{se}	Effective thermal conductivity for solid phase
M_g	Molecular weight for gaseous phase
$\dot{m}$	Mass absorbed per unit volume in unit time
P	Pressure
P_{eq}	Equilibrium pressure
P_d	Desorption pressure
R	Radius of the reactor
S	Solid-gas exchange area
$\dot{q}$	Source term
T	Temperature
T_g	Temperature of gas
T_f	Temperature of cooling fluid
T_{ref}	Reference temperature
T_s	Temperature of solid
T_0	Initial temperature

V_{cv}	Volume of control volume
V_r	Velocity along r direction
V_z	Velocity along z direction
ΔH^0	Reaction heat of formation
ΔS	Enthalpy change for absorption reaction
ε	Porosity
μ	Dynamic viscosity
ρ_g	Density of gaseous phase
ρ_s	Density of solid phase
ρ_{ss}	Density of saturated solid
ρ_0	Initial density
MATLAB	Matrix Laboratory (an engineering software)

1. INTRODUCTION

1.1. General

In recent years the world has confronted environmental problems such as air pollution and global warming which causes serious health problems not only in the current living beings but also in the future generations. The increasing energy demand in industrialized and developing countries makes them the major contributors of problems due to emissions of toxic gases. Depletion of fossil fuels and drawbacks of combustion of these energy sources have shown clearly that changeover towards sustainable energies can no longer be avoided.

In this perspective one of the leading visions in sustainable energy systems is the vision of hydrogen economy. "There is no universally accepted definition of the hydrogen economy, but it is generally viewed as the replacement of the vast majority of petroleum fuels by transportation vehicles of all kinds (automobiles, trucks, trains, and aircrafts) with hydrogen that is burned in internal combustion (IC) engines, external-combustion (jet) engines, or preferably, used in fuel cells to more efficiently generate power for transportation."[1].

Hydrogen, being the lightest element, has been recognized as a secondary form of energy which means an energy carrier rather than a primary energy existing freely in nature. In future energy systems hydrogen is expected to take the role of enabling the use of sustainable energy sources such as hydropower, biomass, wind, and solar [2]. When integrated in renewable sources, as an energy carrier hydrogen will maintain the goals of clean and efficient energy production. For instance the energy carried by hydrogen can be transformed into mechanical or electrical energy with high efficiencies (50-60 %) when used in a fuel cell, without the emission of CO_2 or pollutants [3]. The pathways that access the produced hydrogen to the utilization by consumer is shown schematically in Figure 1.1.
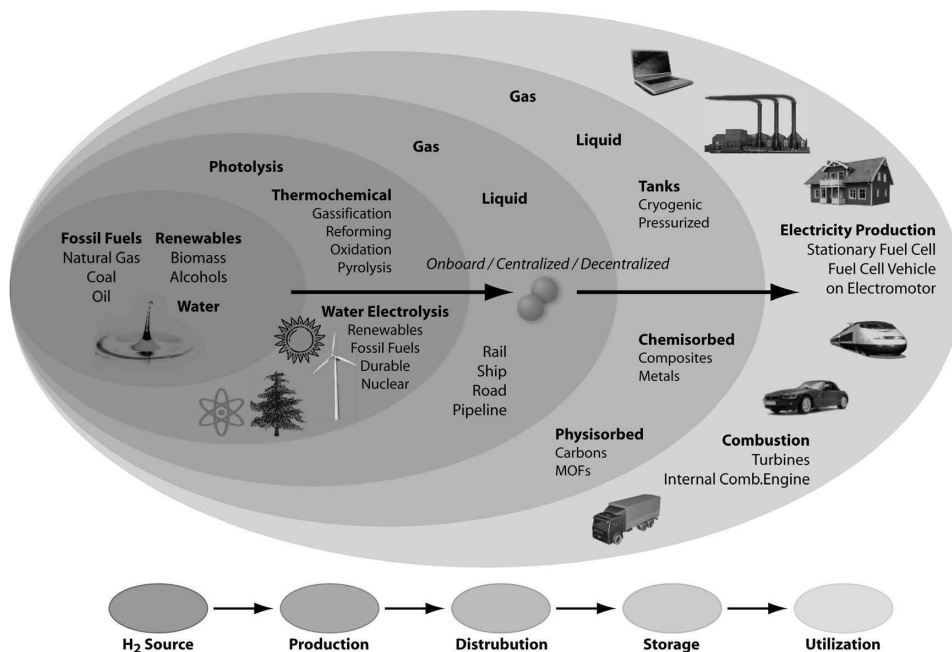
Figure 1.1. Schematic overview from "well-to-wheel" [4]

In order to realize the full potential of hydrogen economy, the challenges of production, storage and distribution should be investigated in detail, especially for the transportation sector. Numerous studies are being conducted on improving hydrogen production by making use of sustainable energy sources. The bottleneck in developing hydrogen economy is seen to be its storage. Hydrogen can be stored mainly in three different ways: (i) pressurized gas, (ii) cryogenic liquid, (iii) solid fuel as chemical or physical combination with materials, such as metal hydrides, complex hydrides and carbon materials. All of these storage techniques need thermal management for controlling process temperature which generally fluctuates due to endothermic or exothermic operations. In order to achieve energy efficiency, the entire system should be practical, compact, lightweight for minimizing the parasitic losses [1, 2, 5].

The requirements of gravimetric and volumetric energy densities for vehicle-based hydrogen storage systems is established through the FreedomCAR and Fuel Partnership between DOE, the U.S. Council for Automotive Research (USCAR) and the energy companies. The gravimetric density should be at least 6 wt.% (i.e., 6 kg H_2 in a 100 kg tank) by 2010 and it should be 9 wt.% by 2015. Moreover fast hydrogen fueling processes are foreseen to be needed in order to meet customer expectations. The target

in fueling rate is to 1.5-2.0 kg $H_2/$ min [6].

The technical performance targets for hydrogen storage systems on-board hydrogen storage for light-duty vehicles are summarized in Figure 1.2.

Storage Parameter	Units	2010	2015	Ultimate
System Gravimetric Capacity				
Usable, specific-energy from H_2	kWh/kg	1.5	1.8	2.5
(net useful energy / max system mass) [a]	(kg H_2/kg system)	(0.045)	(0.055)	(0.075)
System Volumetric Capacity				
Usable energy density from H_2	kWh/L	0.9	1.3	2.3
(net useful energy / max system volume)	(kg H_2/L system)	(0.028)	(0.040)	(0.070)
Storage System Cost [b] (and fuel cost)[c]	$/kWh net ($/kg H_2) $/gge at pump	4* (133) 2-3	2* (67) 2-3	TBD* 2-3
Durability / Operability				
Operating ambient temperature [d]	°C	-30/50 (sun)	-40/60 (sun)	-40/60 (sun)
Min/max delivery temperature	°C	-40/85	-40/85	-40/85
Cycle life (1/4 tank to full) [e]	Cycles	1000	1500	1500
Cycle life variation [f]	% of mean (min) at % confidence	90/90	99/90	99/90
Min delivery pressure from storage system; FC = fuel cell, ICE = internal combustion engine	Atm (abs)	4FC / 35 ICE	3FC / 35 ICE	3FC / 35 ICE
Max delivery pressure from storage system [g]	Atm (abs)	100	100	100
Charging / Discharging Rates				
System fill time (for 5 kg H_2)	min (Kg H_2/min)	4.2 min (1.2 kg/min)	3.3 min (1.5 kg/min)	2.5 min (2.0 kg/min)
Minimum full flow rate	(g/s)/kW	0.02	0.02	0.02
Start time to full flow (20 °C) [h]	s	5	5	5
Start time to full flow (-20 °C) [h]	s	15	15	15
Transient response 10%-90% and 90% - 0% [i]	s	0.75	0.75	0.75
Fuel Purity (H_2 from storage) [j]	% H_2	99.99 (dry basis)		
Environmental Health & Safety				
Permeation and leakage [k]	Scc/h	Meets or exceeds applicable standards		
Toxicity	-			
Safety	-			
Loss of useable H_2 [L]	(g/h)/kg H_2 stored	0.1	0.05	0.05

Figure 1.2. Technical System Targets On-Board Hydrogen Storage for Light-Duty Vehicles [6]

*The storage system costs are currently under review and will be changed at a future date. Useful constants: 0.2778kWh/MJ, $\sim$ 33.3kWh/gal gasoline equivalent.

a Generally the "full" mass (including hydrogen) is used, for systems that gain weight, the highest mass during discharge is used.

b 2003 US$; total cost includes any component replacement if needed over 15 years or 150,000 mile life.

c 2005 US\$; includes off-board costs such as liquefaction, compression, regeneration, etc; based on H_2 production cost of \$2 to \$3/gasoline gallon equivalent untaxed, independent of production pathway. d Stated ambient temperature plus full solar load. No allowable performance degradation from -20C to 40C. Allowable degradation outside these limits is TBD.

e Equivalent to 100,000; 200,000; and 300,000 miles respectively (current gasoline tank spec).

f All targets must be achieved at end of life.

g For delivery to the storage system, in the near term, the forecourt should be capable of delivering 10,000 psi (700 bar) compressed hydrogen, liquid hydrogen, or chilled hydrogen (35 to 77 K) and up to 5,000 psi (350 bar). In the long term, it is anticipated that delivery pressures will be reduced to between 50 and 150 atm for solid state storage systems, based on todays knowledge of sodium alanates.

h Flow must initiate within 25% of target time.

i At operating temperature.

j The storage system will not provide any purification, but will receive incoming hydrogen at the purity levels required for the fuel cell. For fuel cell systems, purity meets SAE J2719, Information Report on the Development of a Hydrogen Quality Guideline in Fuel Cell Vehicles. Examples include: total non-particulates, 100 ppm; H_2O, 5 ppm; total hydrocarbons (C1 basis), 2 ppm; O_2, 5 ppm; He, N_2, Ar combined, 100 ppm; CO_2, 1 ppm; CO, 0.2 ppm; total S, 0.004 ppm; formaldehyde (HCHO), 0.01 ppm; formic acid (HCOOH), 0.2 ppm; NH_3, 0.1 ppm; total halogenates, 0.05 ppm; maximum particle size, < 10 μm, particulate concentration, $< 1\mu$g/L H_2. These are subject to change. Note that some storage technologies may produce contaminants for which effects are unknown; these will be addressed as more information becomes available.

k total hydrogen lost into the environment as H_2; relates to hydrogen accumulation in enclosed spaces. Storage system must comply with CSA/NGV2 standards for vehicular tanks. This includes any coating or enclosure that incorporates the envelope of the storage system.

L total hydrogen lost from the storage system, including leaked or vented hydrogen; relates to loss of range [6].

Figure 1.3 shows the current status for system capacity and cost for storage systems. It is noted that the current accomplishments show material-based capacities whereas targets are system-level based which means the material, tank and all balance-of-plant components of the storage system are also considered. The system-level data also includes the first charge of hydrogen as well as any preconditioning such as purification, liquefaction and regeneration of material, particularly for chemical hydrogen storage, for which the cost of regenerating spent fuel will need to be included [6].
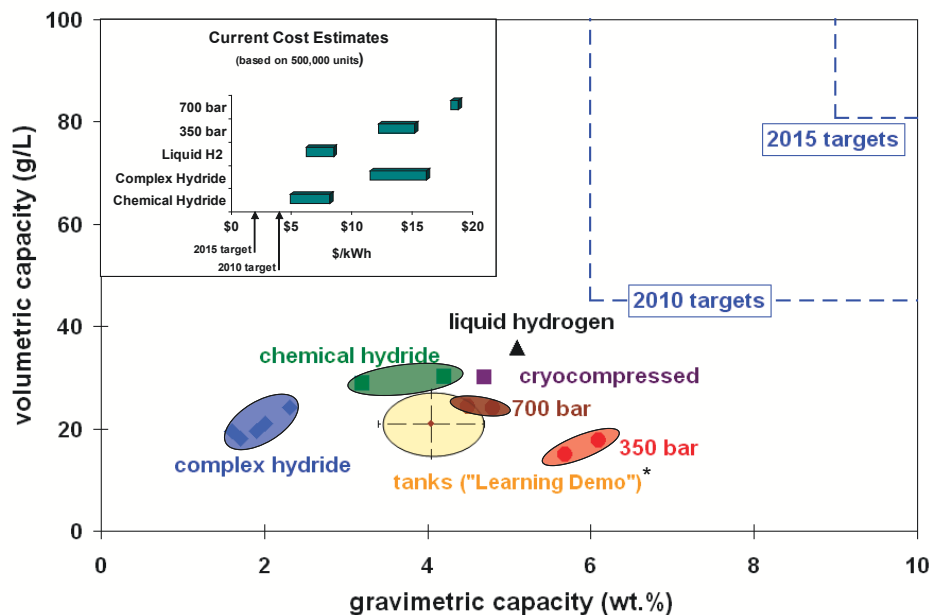
Figure 1.3. Current Status for system Capacity and Cost [6]

Hydrogen has low boiling point (20.13 K) and low density at room temperature (0.0898 g/L). Therefore physical storage of hydrogen as a pressurized gas or in cryogenic liquid, associates significant energy losses, potential security risks and large volumes. In commercially available pressurized gas storage technology, hydrogen is compressed at 350 bar or at 700 bar. The corresponding densities of hydrogen are 22.9 g/L and 39.6 g/L, respectively. Main advantage of this method is simplicity. However the process of compressing of hydrogen at high pressures requires a large amount of energy. Also during fast tank filling at room temperature(1 kg H_2/min) due to Joule-Thomson effect temperature increase of approximately 50 K is observed. Overheating causes decrease in density which is avoided by using other cooling options and extra compression work. In liquid hydrogen storage hydrogen is maintained at cryogenic state (at 20.13 K with

density of 70.8 g/L) and stored in cryogenic tanks at atmospheric pressure. Cryogenic storage is almost twice efficient when compared to compressed hydrogen storage at 700 bar. However the high energy consumption related to liquefaction process and continuous boil-off during storage hampers this technology for storing large amounts of hydrogen for on-board applications [2].

Storing hydrogen in metal compounds appears to be a promising method in dissolving the bottleneck through hydrogen energy. The research on metal-hydrides reveals that these compounds retain remarkable efficiency in hydrogen energy storage and distribution systems. The significance arises from the fact that the employability of metal-hydrides is highly dependent on their heat and mass transfer characteristics, hydriding/dehyriding durations and maximum number of hydriding/dehydriding cycles.

1.2. Review of Metal Hydrides

The family tree for materials that reversibly absorb hydrogen is shown schematically in Figure 1.4 where TM is used for transition metal [7].
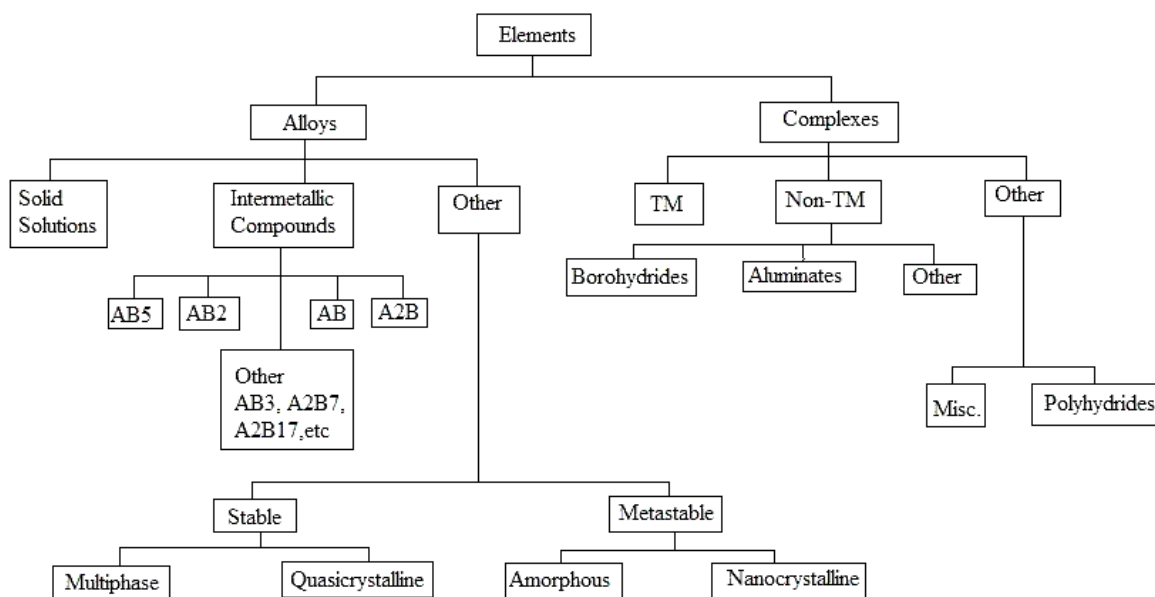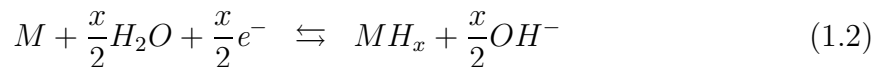

Figure 1.4. Family Tree of Hydriding Alloys and Complexes [7]

The broad family of metal hydrides experiences hydriding and dehydriding reactions by two ways: (i) dissociative chemisorption of H_2, (ii) electrochemical splitting of H_2O.

$$M + \frac{x}{2}H_2 \quad \leftrightarrows \quad MH_x \tag{1.1}$$

$$M + \frac{x}{2}H_2O + \frac{x}{2}e^- \quad \leftrightarrows \quad MH_x + \frac{x}{2}OH^- \tag{1.2}$$

where M represents the metal.

Two different kinds of hydrides are formed in host lattice purveyed by metal beds. At α phase hydrogen is absorbed, and at β phase hydride is fully comprised. Hydrogen storage on metal is highly dependent on metal's ability to dissociate hydrogen which is correlated to surface structure, morphology, and purity. The properties of an optimum hydrogen storage metal is generally stated as; high hydrogen capacity per unit mass and unit volume which determines the amount of available energy, low dissociation temperature, moderate dissociation pressure, low heat of formation in order to minimize the energy necessary for hydrogen release, low heat dissipation during the exothermic hydride formation, reversibility, limited energy loss during charge and discharge of hydrogen, fast kinetics, high stability against O_2 and moisture for long cycle life, cyclibility, low cost of recycling and charging infrastructures and high safety [5].

In Pressure-Composition-Temperature (PCT) relations of metal hydrides, isothermal Pressure-Composition loops take important role. The plateau pressure represents the coexistence of two condensed phases when solubility of hydrogen in lattice is achieved. Most of the conventional metal hydrides do not show flat plateau pressure and zero hysteresis [7, 9]. In Figure 1.5 isothermal P-C curve for a metal hydride system is given.
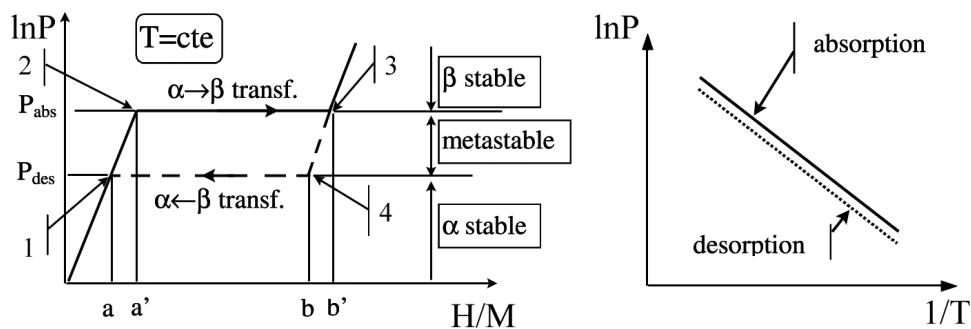
Figure 1.5. Isothermal Hysteresis (left), 12 and 34=reversible paths; 23 and
41=irreversible paths; Effect of Hysteresis on Vant Hoff Plot (right) [9]

The effect of temperature change is related to plateau pressure by Van't Hoff
relation given in Equation 1.3.

$$lnP = \frac{\Delta H}{RT} - \frac{\Delta S}{R}$$
(1.3)

where ΔH and ΔS are enthalpy and entropy changes during hydriding reaction, re-
spectively. T is the absolute temperature of the instantaneous metal bed.

1.2.1. Elements

Most of the natural elements hydride reversibly. Elemental hydrides for chemi-
cal storage are listed periodically in Figure 1.6. Due to weight constraints of mobile
applications the first four periods of elements are suitable for potential storage. The
range of hydrogen contamination among these elements is 1.9% (VH)-13 % (LiH). Hy-
drogenation of the first group hydrides is irreversible under practical conditions [8].

	I	II	III	IV	V	VI	VII	VIII	IX	X	XI	XII	XIII	XIV	XV	XVI	XVII	XVIII
1	H																	He
2	LiH 12.7	BeH$_2$ 18.3	*Ionic Hydrides*										BH$_3$ 21.9	CH$_4$ 25.1	NH$_3$ 17.8	H$_2$O 11.2	HF 5.0	Ne
3	NaH 4.2	MgH$_2$ 7.7	*Metallic Hydrides*								*Covalent Polymeric Hydrides*		AlH$_3$ 10.1	SiH$_4$ 12.6	PH$_3$ 8.9	H$_2$S 5.9	HCl 2.8	Ar
4	KH 2.5	CaH$_2$ 4.8	ScH$_2$ 4.3	TiH$_2$ 4.0	VH$_{1/2}$ 1.9/3.8	CrH$_{1/2}$ 1.9/3.7	Mn	Fe	Co	NiH$_{<1}$ <1.7	CuH 1.6	ZnH$_2$ 3.0	*GaH$_3$* 4.2	GeH$_4$ 5.3	AsH$_3$ 3.9	H$_2$Se 2.5	HBr 1.2	Kr
5	RbH 1.2	SrH$_2$ 2.2	YH$_{2/3}$ 2.2/3.3	ZrH$_2$ 2.2	*NbH$_2$* 2.1	Mo	Tc	Ru	Rh	PdH$_{<1}$ <0.9	Ag	*CdH$_2$* 1.8	*InH$_3$* 2.6	SnH$_4$ 3.3	SbH$_3$ 2.4	H$_2$Te 1.6	HI 0.8	Xe
6	CsH 0.8	BaH$_2$ 1.4	LaH$_{2/3}$ 1.4/2.1	HfH$_2$ 1.1	TaH 0.6	W	Re	Os	Ir	Pt	*AuH$_3$* 1.5	*HgH$_2$* 1.0	*TlH$_3$* 1.5	PbH$_4$ 1.9	BiH$_3$ 1.4	H$_2$Po 1.0	HAt 0.5	Rn
7	Fr	Ra	AcH$_2$ 0.9															

Covalent Hydrides

Figure 1.6. Elemental Hydrides and Corresponding Hydrogen Absorbed Weight Percent [8]

PCT properties of elemental hydrides are given by Van't Hoff lines in Figure 1.7. For practical applications the desired range dissociation pressure and temperature are 1-10 atm and 0-100 °C, respectively. Only VH$_2$ is seen to be a potential storage material [7].
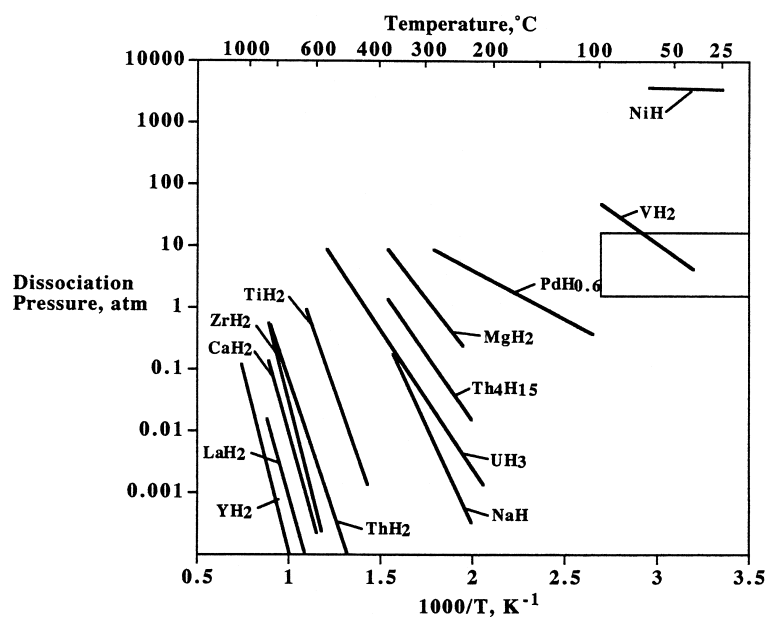

Figure 1.7. Vant Hoff Lines (desorption) For Elemental Hydrides [7]

1.2.2. Alloys

Among the group of alloys the most prior research has been conducted on inter-metallic compounds (IMC). In IMC's a strong hydriding metal element A is combined with a weak hydriding element B in order to form a compound which has desired intermediate thermodynamic affinities for hydrogen. Most of the conventional metal hydrides consist of IMC's such as $LaNi_5$, $ZrMn_2$, TiFe, Mg_2Ni which are grouped as AB_5, AB_2, AB, AB_2 intermetallic compounds, respectively.[2].

The extraordinary feature of interpolating the extremes of elemental hydrides results in conventional reversible metal hydrides. An example of this is explained in Table 1.1 where P_d is the desorption pressure given at 25 °C.

Table 1.1. Some Properties of Reversible Metal Hydrides [7]

Element Metal	Hydrided Compound	P_d(atm)	ΔH_f (kJ/mol H_2)
La	LaH_2	3×10^{-29}	-208
Ni	NiH	3400	-8.8
$LaNi_5$	$LaNi_5H_6$	1.6	-30.9

In this study the hydriding and dehydriding processes of $LaNi_5$ is investigated which is one of the mostly studied member of AB_5 group IMC's. This group compounds generally have hexagonal crystal structure. A elements can be one of the lanthanides, Ca, Y, Zr whereas B elements are generally Ni, Co, Al, Mn, Fe, Cu, Sn, Si, Ti. Various numerical studies can also be found on AB_5 alloys based on lanthanide mixture mischmetal (Mm) which means for both A and B parts, mixture of the mentioned elements is combined in order to reduce the cost of the metal bed [7]. PCT properties of some of the AB_5 IMC's are given by Van't Hoff lines in Figure 1.8.
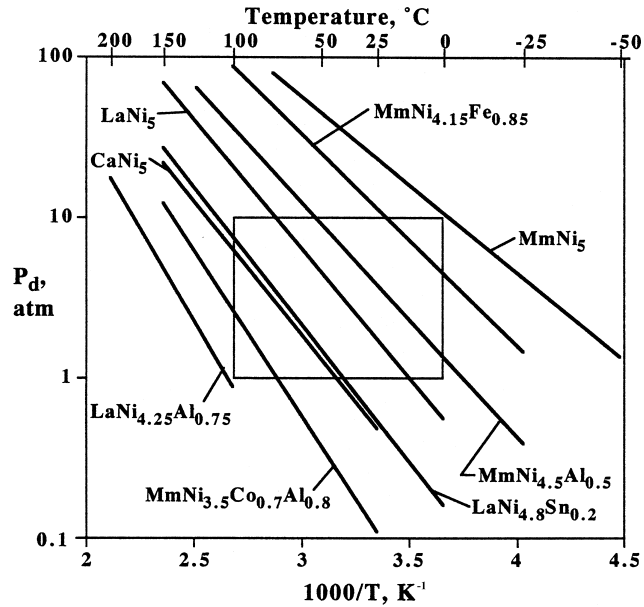
Figure 1.8. Vant Hoff Lines For various AB_5 Hydrides [7]

AB$_5$ IMC's mostly activate at room temperature. On the first hydriding/dehydriding cycle they break into fine powder which makes them mildly phyrophoric therefore AB$_5$ alloys do not easily form protective oxide layers. This makes them tolerable to small amounts of impurities. When compared to other groups of IMC's AB$_5$ group compounds are generally better at heat transfer [7].

Numerous studies on this topic verify the goal of attaining an optimum mathematical model that represents the physical phenomena in the most realistic and accurate way. Therefore different approaches with different assumptions are experienced. Various commercially available software packages have also been used for numerical modelling.

1.3. Literature Survey

The study of hydrogen storage in a metal hydride bed is an example of solving heat and mass transfer equations of a chemical reaction in a porous medium simultaneously. In the literature there exists numerous studies on the process of hydriding and dehydriding which are conducted numerically and/or experimentally. Lucas and Richards [10] developed a one dimensional model to simulate the heat transfer characteristics of absorption and desorption processes of a commercially available containment vessel. In this primary study the time to absorb or desorb hydrogen is predicted. But the model mainly lacks the source term that originates from the heat generation during the absorption process. Mayer et al. [11] studied heat and mass transfer equations; they assumed the local gas and solid temperatures are equal (LTE) and gas pressure is constant in the reactor. Their experimental results showed that the reactor geometry affects temperature distribution. The temperature profiles varied not only with radial direction but also with longitudinal direction. Jemni and Nasarallah [12] developed two dimensional mathematical model. Unsteady heat and mass transfer during absorption is solved numerically with finite domains method which is stated in [13]. Since the reactor consists of a solid phase (metal-hydride) and of a gaseous phase (hydrogen), two phase discontinuous porous medium conditions are concerned as described in [14]. They showed that the reactor geometry, inlet pressure and inlet temperature are important parameters during absorption whereas convective terms in the energy balance equation are insignificant. Jemni et al. added to these findings that the hypothesis of thermal equilibrium is valid in hydriding and dehydriding processes [15]. Furthermore it is proved that the effect of pressure variation is also negligible. Nakagawa et al. [16] verified the validity of the assumptions such as neglecting convective term in an energy equation for gas phase and assuming local thermal equilibrium in the hydriding bed. They also derived the thermophysical properties such as; thermal conductivity, specific heat, particle diameter of metal hydride as a function of reaction kinetics which is also developed by their colleagues Inomata et al. [17]. Mat et al. [18] studied metal hydride formation based on Jemni and Nasrallah's continuum mathematical model and concluded that absorption process is faster at the initial times then slows down since the temperature of reaction bed increases due to heat of formation. Aldas et al. [19]

evaluated the three dimensional model and investigated heat and mass transfer, fluid flow and chemical reactions in the hydride bed. They found that hydride formation is highly dependent on temperature distribution. Although fluid flow has influence on temperature profile, overall hydride formation is not affected by fluid flow. Demircan et al. [20] studied the same phenomena with two different geometries. They showed that the one with more heat transfer reaches same hydriding percentage in a significantly shorter time interval. Kikkinides et al. [21] conducted studies on optimization of metal hydride beds. Their main concern was reducing storage time by changing parameters of cooling system design and cooling fluid temperature.

2. THEORY

2.1. Metal Hydride Reactor Geometry

Metal hydride reactors are generally cylindrical tubes containing the metal pow-der inside, which exchanges heat through lateral and base areas. There exists a cooling fluid around the container. The orientation of convecting fluid around the metal hy-dride cylinder can change for different reactor geometries.

In most experimental setups there exists a ball mill section dedicated to producing fine particles and a vacuum pump to evacuate the container where the reaction takes place in order to prevent undesired compounds to be formed by interacting oxygen with the metal surface. To compare the results of the theoretical model with the data obtained from the experimental setup thermocouple and pressure transducers are inserted at certain locations in the metal-hydride. An example of an experimental setup used for investigating hydriding or dehydriding characteristics of a metal hydride is given in Figure 2.1.
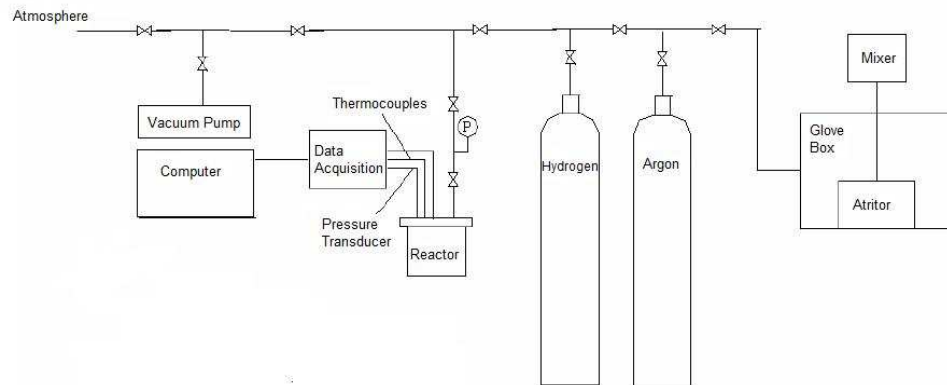
Figure 2.1. Experimental Setup for Metal Hydride Reactors [22]

Before the experimental part to start, activation process of $LaNi_5$ should be com-pleted. The required parameters are optional for different setups but mainly the grind-ing of $LaNi_5$ takes place until the particle diameter reduces to 3-10 μm, the processed material is transferred to the reaction chamber in the presence of a non-reacting gaseous medium, the reactor is heated and cooled down several times. Hydrogen is pressed into

the chamber at constant pressure or at constant mass flow rates.

Thermal properties of the metal hydride beds limit the hydriding time. During hydriding the temperature of the metal hydride bed increases dramatically due to the release of the heat of formation. This rise has an inverse effect in effective thermal conductivity. The decrease in effective thermal conductivity impedes the removal of heat from the medium. This cycle will eventually end in stalling or reversing the process. In order to enhance heat transfer from the hydride bed to the cooling fluid, different geometries are being investigated.

2.2. Mathematical Model

In the literature there exists two different approaches to the heat and mass transfer analysis in metal-hydride reactors.

i. Non-LTE approach: The two phases, solid (metal hydride bed) and fluid (hydrogen gas), in the medium are not at equal temperature at each time interval.
ii. LTE approach: The two phases are assumed to be locally equal at each time interval.

In non-LTE approach two energy balance equations are derived which are for fluid and solid phases separately. The boundary condition at the inlet of the reactor is where these two are coupled. The fundamental analysis of two phase reactions are considered with respect to the first approach. However LTE approach is used in most of the recent studies on investigation of hydrogen absorption in $LaNi_5$. The validity of LTE approach is proved by Jemni et al [15] for both absorption and desorption processes. They have also shown that local thermal equilibrium assumption has no effect on calculation of total hydrogen mass that is absorbed or desorbed.

In this study the hydriding phenomena of a lanthanite based intermetallic compound will be investigated from the perspective of heat and mass transfer issues. Therefore firstly the most general case with non-LTE approach is clarified. Then in the light

of supporting articles on the validity of LTE approach, the governing filed equations are constituted for solving the hydriding case of LaNi$_5$ based on LTE approach.

2.2.1. Energy Equation

The differential equations governing the hydriding and dehydriding processes in the cylindrical tube are defined to be:

For fluid phase:

$$\varepsilon \rho_g C_{pg} \frac{\partial T_g}{\partial t} = \frac{1}{r}\frac{\partial}{\partial r}\left(\varepsilon r k_{ge}\frac{\partial T_g}{\partial r}\right) + \frac{\partial}{\partial z}\left(\varepsilon k_{ge}\frac{\partial T_g}{\partial z}\right) - (\rho C_{pg}V_{gr})\frac{\partial T_g}{\partial r}$$

$$-(\rho C_{pg}V_{gz})\frac{\partial T_g}{\partial z} - h_{gs}(T_g - T_s)S - max(-\dot{m},0)C_{pg}(T_g - T_s) \quad (2.1)$$

where ε, k_{ge}, h_{gs} represent porosity of the metal-hydride bed, effective thermal conductivity of gaseous phase and convection heat transfer coefficient between solid and gas, respectively.

For solid phase:

$$(1-\varepsilon)\rho_s C_{ps}\frac{\partial T_s}{\partial t} = \frac{1}{r}\frac{\partial}{\partial r}\left((1-\varepsilon)r k_{se}\frac{\partial T_s}{\partial r}\right) + \frac{\partial}{\partial z}\left((1-\varepsilon)k_{ge}\frac{\partial T_s}{\partial z}\right) \quad (2.2)$$

$$-h_{gs}(T_g - T_s)S - \dot{m}(\Delta H^o + C_{ps}T_s - C_{pg}T_g)$$

where k_{se}, ΔH^o are effective thermal conductivity of solid phase and heat of formation of the process.

- Initial condition:

$$T_g(z, r, 0) \quad = \quad T_0 \qquad (2.3)$$

$$T_s(z, r, 0) \quad = \quad T_0 \qquad (2.4)$$

- Boundary Conditions:
  - At the reactor inlet the temperature of gas is assumed to be constant.

$$T_g(H, r, t) = T_0 \qquad (2.5)$$

Also the gas and solid phases are tied with the below equation.[12]

$$-k_{se}\frac{\partial T_s}{\partial z}(H, r, t) = h_{gs}(T_s - T_g) \qquad (2.6)$$

  - The problem is radially symmetric. Therefore boundary conditions at $r = 0$ are stated as such:

    for fluid:

$$\frac{\partial T_g}{\partial r}(z, 0, t) = 0 \qquad (2.7)$$

    for solid:

$$\frac{\partial T_s}{\partial r}(z, 0, t) = 0 \qquad (2.8)$$

  - Convective boundary conditions are valid for the base and lateral areas:

    for fluid;

$$-k_{ge}\frac{\partial T_g}{\partial r}(z, R, t) \quad = \quad h(T_g - T_f) \qquad (2.9)$$

$$-k_{ge}\frac{\partial T_g}{\partial z}(0, r, t) \quad = \quad h(T_g - T_f) \qquad (2.10)$$

for solid;

$$-k_{se}\frac{\partial T_s}{\partial r}(z, R, t) = h(T_s - T_f) \tag{2.11}$$

$$-k_{se}\frac{\partial T_s}{\partial z}(0, r, t) = h(T_s - T_f) \tag{2.12}$$

where h is the conductance between hydride bed and cooling fluid and T_f is the temperature of the cooling fluid.

2.2.2. Mass Balance Equation

Mass balance equation for hydrogen:

$$\varepsilon\frac{\partial \rho_g}{\partial t} + \frac{1}{r}\frac{\partial(r\rho_g V_r)}{\partial r} + \frac{\partial(\rho_g V_z)}{\partial z} = -\dot{m} \tag{2.13}$$

Mass balance equation for metal:

$$(1 - \varepsilon)\frac{\partial \rho_s}{\partial t} = \dot{m} \tag{2.14}$$

• Initial hydride mass condition

$$\rho_s = \rho_0 \tag{2.15}$$

2.2.3. Momentum Equation

Momentum equation in z direction:

$$\rho\frac{\partial V_z}{\partial t} = -\frac{\partial P}{\partial z} + \mu\left(\frac{1}{r}\frac{\partial}{\partial r}\left(r\frac{\partial V_z}{\partial r}\right) + \frac{\partial^2 V_z}{\partial z^2}\right) - \rho\left(V_r\frac{\partial V_z}{\partial r} + V_z\frac{\partial V_z}{\partial z}\right) \qquad (2.16)$$

Momentum equation in r direction:

$$\rho\frac{\partial V_r}{\partial t} = -\frac{\partial P}{\partial r} + \mu\left(\frac{\partial}{\partial r}\left(\frac{1}{r}\frac{\partial}{\partial r}(rV_r)\right) + \frac{\partial^2 V_r}{\partial z^2}\right) - \rho\left(V_r\frac{\partial V_r}{\partial r} + V_z\frac{\partial V_r}{\partial z}\right) \qquad (2.17)$$

where V_z and V_r are the velocity component of the hydrogen in z and r directions respectively.

In literature ([12], [15]) it is seen that momentum equations are also expressed through Darcy's Law.

$$\vec{V} = -\frac{K}{\eta}grad P_g \qquad (2.18)$$

where K represents permeability and η represents viscosity of hydrogen. In most of the studies permeabilty is considered to be constant whereas Nakagawa et al [16] stated permeability as a function of particle diameter, porosity, mean free path of hydrogen atom.

- Initial conditions:

$$P_g(z, r, 0) \;=\; P_0 \qquad (2.19)$$

$$V_r \;=\; 0 \qquad (2.20)$$

$$V_z \;=\; 0 \qquad (2.21)$$

- Boundary Conditions:

  - The problem is symmetric with respect to z-direction.

$$\frac{\partial P_g}{\partial r}(z, 0, t) = 0 \tag{2.22}$$

  - The base and lateral surfaces are assumed to be impervious and no-slip conditions are valid therein. Inlet hydrogen pressure is assumed to be constant.

$$\frac{\partial P_g}{\partial r}(z, R, t) = 0 \tag{2.23}$$

$$\frac{\partial P_g}{\partial z}(0, r, t) = 0 \tag{2.24}$$

$$P_g(H, r, t) = P_0 \tag{2.25}$$

2.2.4. Reaction Kinetics

Mayer et al [11] expressed the hydrogen mass absorbed or desorbed per unit volume and per unit time by the term $\dot{m}$.

- For hydriding case:

$$\dot{m} = C_a \exp\left(-\frac{E_a}{RT_s}\right) \ln\left(\frac{P_g}{P_{eq}}\right)(\rho_{ss} - \rho_s) \tag{2.26}$$

where C_a is material dependent constant for absorption process, E_a is the activation energy for absorption, ρ_{ss} is the density of hydride at saturation and P_{eq} is the equilibrium pressure of hydrogen.

- For dehydriding case:

$$\dot{m} = C_d \exp\left(-\frac{E_d}{RT_s}\right)\left(\frac{P_g - P_{eq}}{P_{eq}}\right)(\rho_{ss} - \rho_s) \tag{2.27}$$

where C_d is material dependent constant for desorption process, E_d is the activation energy for desorption.

Equilibrium pressure is a function of temperature and hydrogen to metal atomic ratio given in [23].

$$P_{eq} = f\left(\frac{H}{M}\right) \exp\left(\frac{\Delta H}{R}\left(\frac{1}{T} - \frac{1}{T_{ref}}\right)\right) \tag{2.28}$$

3. PROBLEM DESCRIPTION AND NUMERICAL METHODS

3.1. Objective

The aim of this study is to investigate hydrogen storage in metal-hydride reactors from the thermodynamic point of view. The analysis is based on evaluating temperature profiles and total mass of hydrogen that is absorbed during hydriding reaction.

The significance of this problem arises from the fact that the employability of metal-hydrides are highly dependent on their heat and mass transfer characteristics, hydriding/dehyriding durations and maximum number of hydriding/dehydriding cycles. The numerous studies on this topic verify the goal of attaining an optimum mathematical model that represents the physical phenomena in the most realistic and accurate way. Therefore different approaches with different assumptions are experienced. Various commercially available software packages have also been used for numerical modelling.

In this study a mathematical model which governs heat and mass transfer characteristics of hydrogen absorption in LaNi$_5$ is studied. A numerical model is developed based on finite difference method. The analysis is conducted using MATLAB. Evaluation of temperature profiles and hydrogen mass that is being absorbed during hydriding are shown to be consistent with the experimental data and with the previous numerical studies.

3.2. Governing Field Equations

Cylindrical reaction bed filled with LaNi$_5$ metal, is surrounded by a convecting fluid which is in circulation at constant temperature. The cooling fluid is assumed to be water which is at room temperature. From the inlet of the reactor hydrogen gas is compressed to the metal-hydride bed. Hydrogen gas is compressed through the reactor

inlet into the metal hydride bed. Reactor geometry is chosen to be the one given in figure 3.1.
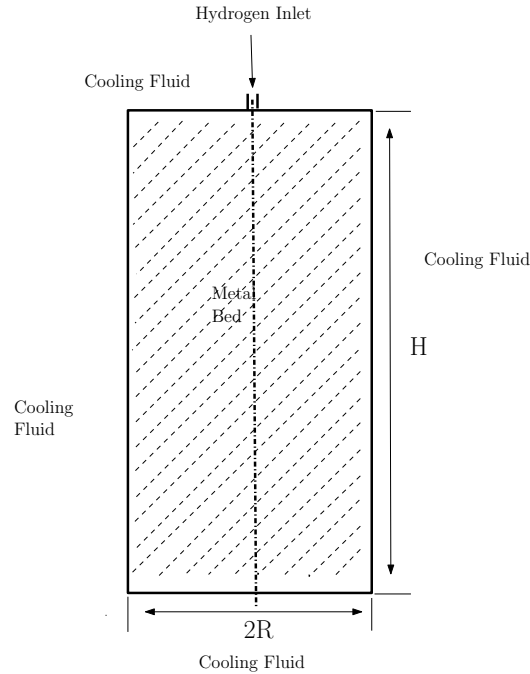

Figure 3.1. Schematic sketch of metal-hydride reactor

3.2.1. Assumptions

- The solid and gas phases are in thermal equilibrium locally.
- Conductive model is used for heat transfer analysis of the metal-hydride bed which is mainly neglecting the heat transport by convection.
- Effective thermal conductivity, k_e is considered to be constant throughout hydriding process.
- The effect of hydrogen concentration, (H/M), on the equilibrium pressure is neglected. The Van't Hoff equation is assumed to be valid for expressing equilibrium pressure.
- Pressure drop along the cylinder is neglected.
- Hydrogen gas is considered as an ideal gas.
- Boundary walls of the reactor are impermeable.

3.2.2. Energy Balance in LTE

The differential equations governing the hydriding processes in the cylindrical tube are defined to be:

$$(\rho C_p)_e \frac{\partial T}{\partial t} = \frac{1}{r}\frac{\partial}{\partial r}\left(rk_e\frac{\partial T}{\partial r}\right) + \frac{\partial}{\partial z}\left(k_e\frac{\partial T}{\partial z}\right) - \dot{m}(\Delta H^o + T(C_{pg} - C_{ps})) \quad (3.1)$$

where

$$(\rho C_p)_e = (\varepsilon\rho_g C_{pg} + (1-\varepsilon)\rho_s C_{ps}) \quad (3.2)$$

and k_e is the effective thermal conductivity of the metal-hydride bed which is expressed as:

$$k_e = \varepsilon k_g + (1-\varepsilon)k_s \quad (3.3)$$

3.2.3. Mass Balance in LTE

The value of ρ_g in Equation 3.2 is obtained from ideal gas law. and the value for ρ_s is obtained by solving mass balance equation instantaneously.

$$\rho_g = \frac{M_g P_g}{RT} \quad (3.4)$$

The value for ρ_s in Equation 3.2 is obtained by solving mass balance equation simultaneously.

$$(1-\varepsilon)\frac{\partial\rho_s}{\partial t} = \dot{m} \quad (3.5)$$

The density of the metal increases as it reacts with hydrogen and reaches to a maximum when the metal is totally hydrided. For instance for $LaNi_5$, it is achieved when $H/M = 6$ (hydrogen to metal atomic ratio) or in other words when $\rho_s = \rho_{ss}$.

This causes parabolic profile distribution for the term $\dot{m}$. Therefore coupling of mass balance equations with energy balance equations is significant when evaluating not only total mass of hydrogen that is absorbed but also temperature distributions during absorption.

- Initial hydride mass condition

  $\rho_s = \rho_0$ where for LaNi$_5$which has 0.5 porosity , $\rho_0 = 8400 kg/m^3$.

- Initial condition:

$$T(z,r,0) \;=\; T_0 \tag{3.6}$$

$$\rho_s \;=\; \rho_0 \tag{3.7}$$

Since pressure drop along the tube is neglected. The pressure of gas around each node is assumed to be the same as the pressure of hydrogen in the entrance of the tank.

$$P_g \;=\; P_0 \tag{3.8}$$

- Boundary Conditions:

  At the reactor inlet $(z = H)$ convective boundary condition is applied.

$$-k_e \frac{\partial T}{\partial z}(H,r,t) = h(T - T_f) \tag{3.9}$$

At $r = 0$ the problem is symmetric.

$$\frac{\partial T}{\partial r}(z,0,t) = 0 \tag{3.10}$$

At the bottom of the reactor $(z = 0)$;

$$-k_e \frac{\partial T}{\partial z}(0, r, t) = h(T_f - T) \tag{3.11}$$

At the lateral areas$(r = R)$;

$$-k_e \frac{\partial T}{\partial r}(z, R, t) = h(T - T_f) \tag{3.12}$$

where h is the conductance between hydride bed and cooling fluid and T_f is the temperature of the cooling fluid.

3.2.4. Reaction Kinetics for Hydriding of LaNi$_5$

The experimental parameters for hydrogen mass absorbed per unit volume per time is obtained from the studies of Suda et al [24].

$$\dot{m} = C_a \exp\left(-\frac{E_a}{RT_s}\right) ln\left(\frac{P_g}{P_{eq}}\right)(\rho_{ss} - \rho_s) \tag{3.13}$$

C_a is the reaction constant and E_a is the activation energy which are 59.187 1/s and $21,179$ J/mol, respectively [25].

Since the analysis are evaluated for LTE conditions T_s is the value found for fluid and solid phase. Also P_g is the pressure at which the hydrogen is compressed into the reaction bed.

As explained in 2.2.4 the equilibrium pressure is assumed to be independent from H/M ratio therefore it is expressed with Van't Hoff equation.

$$P_{eq} = \exp\left(A - \frac{B}{T}\right) \tag{3.14}$$

where $A = 17.58$ and $B = 3635$ [27].

3.3. Numerical Methods

The assumption of constant effective thermal conductivity throughout the hydriding process simplifies the energy balance equations as follows:

$$
\begin{aligned}
(\rho C_p)_e \frac{\partial T}{\partial t} &= k\nabla^2 T + \dot{q} \\
(\rho C_p)_e \frac{\partial T}{\partial t} &= \frac{k}{r}\frac{\partial T}{\partial r} + k\frac{\partial^2 T}{\partial r^2} + k\frac{\partial^2 T}{\partial z^2} + \dot{q}
\end{aligned}
\tag{3.15}
$$

where source is defined as

$$
\dot{q} = \left(C_a \exp\left(-\frac{E_a}{RT_{i,j}^p} \right) ln\left(\frac{P_g}{P_{eq}} \right) (\rho_{ss} - \rho_s) \right) (\Delta H^o + T_{i,j}^p (C_{pg} - Cps))
\tag{3.16}
$$

and

$$
P_{eq} = \exp\left(A - \frac{B}{T_{i,j}^p} \right)
\tag{3.17}
$$

These are coupled to the mass balance Equation [3.5] for the metal hydride.

In the literature it is observed that continuum models based on finite domains method given in [13] is mostly studied. Patankar proposes a discretization concept which has bases on finite difference method but employs ideas that are related to finite element methodology. Most of the previous studies apply Patankar's discretization in the implicit scheme.

In this study energy balance method is used for discretizing the heat equation. Mainly transient heat conduction with convective boundary conditions is evaluated in explicit scheme. For the studied geometry there exist nine types of critical nodes at which the discretization equations vary with respect to the volume that the nodes are located in and to their neighboring nodes that contribute to the energy balance equation for each one.

3.3.1. Discretization of the Field Equations

The explicit finite difference equations are derived for nine different nodes by applying energy balances to appropriate control volumes. Our selection of cylindrical geometry reduces the problem to be two dimensional. Therefore the relevant control volumes are basically rings with different radii and heights. The energy balance equations for each type of control volume is given after the figure of the nodes located on a schematic drawing of slide of the cylindrical tank.

- For any interior node
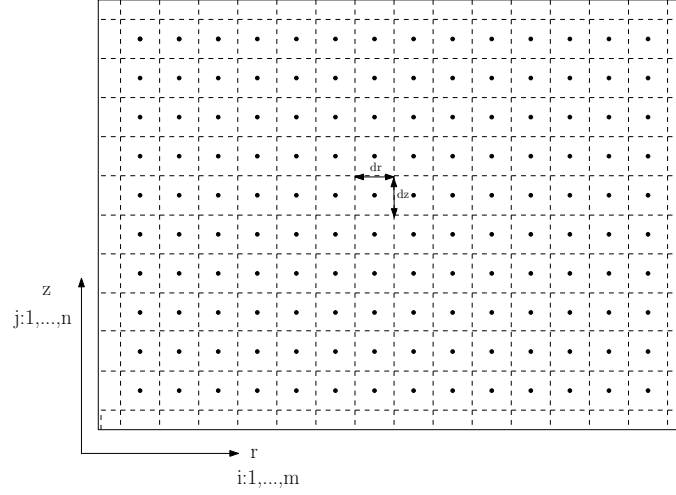
Figure 3.2. Location of interior nodes

The number of nodes along z and r directions are n and m respectively. The assumption of constant effective thermal conductivity throughout the hydriding process simplifies the energy balance equation for any interior node as follows:

$$V_{cv} = 2\pi i (\Delta r)^2 \Delta z \tag{3.18}$$

$$(\rho C_p)_e V_{cv}\left(\frac{T_{i,j}^{p+1} - T_{i,j}^p}{\Delta t}\right) = k2\pi (i - \frac{1}{2})\Delta r \Delta z \left(\frac{T_{i-1,j}^p - T_{i,j}^p}{\Delta r}\right)$$

$$+ k2\pi (i + \frac{1}{2})\Delta r \Delta z \left(\frac{T_{i+1,j}^p - T_{i,j}^p}{\Delta r}\right)$$

$$+ k2\pi i \Delta r \Delta r \left(\frac{T_{i,j+1}^p - T_{i,j}^p}{\Delta z}\right)$$

$$+ k2\pi i \Delta r \Delta r \left(\frac{T_{i,j-1}^p - T_{i,j}^p}{\Delta z}\right)$$

$$+ \dot{q}V_{cv} \tag{3.19}$$

- For a node on the symmetry axis at $r = 0$ excluding the ones on the boundaries
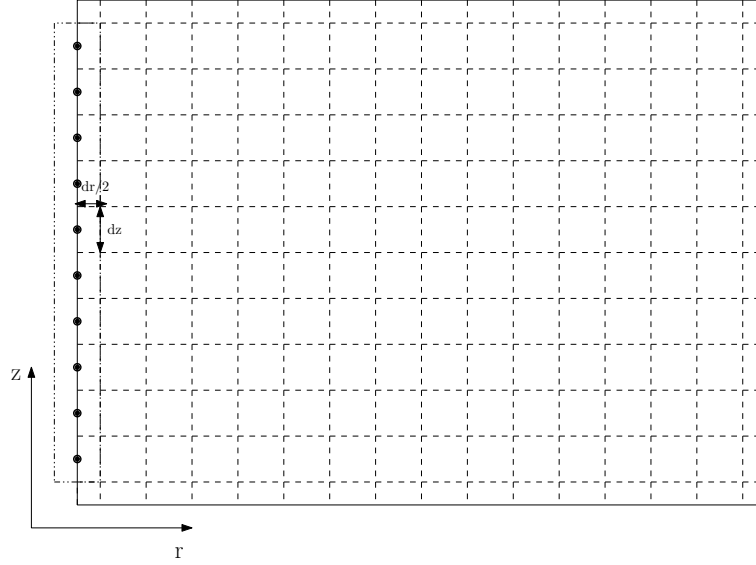

Figure 3.3. Location of nodes on symmetry axis

$$V_{cv} = \pi \left(\frac{\Delta r}{2}\right)^2 \Delta z \tag{3.20}$$

$$(\rho C_p)_e V_{cv} \left(\frac{T_{1,j}^{p+1} - T_{1,j}^p}{\Delta t}\right) = k 2\pi \left(\frac{\Delta r}{2}\right) \Delta z \left(\frac{T_{2,j}^p - T_{1,j}^p}{\Delta r}\right)$$

$$+ k\pi \left(\frac{\Delta r}{2}\right)^2 \left(\frac{T_{1,j-1}^p - T_{1,j}^p}{\Delta z}\right)$$

$$+ k\pi \left(\frac{\Delta r}{2}\right)^2 \left(\frac{T_{1,j+1}^p - T_{1,j}^p}{\Delta z}\right)$$

$$+ \dot{q} V_{cv} \tag{3.21}$$

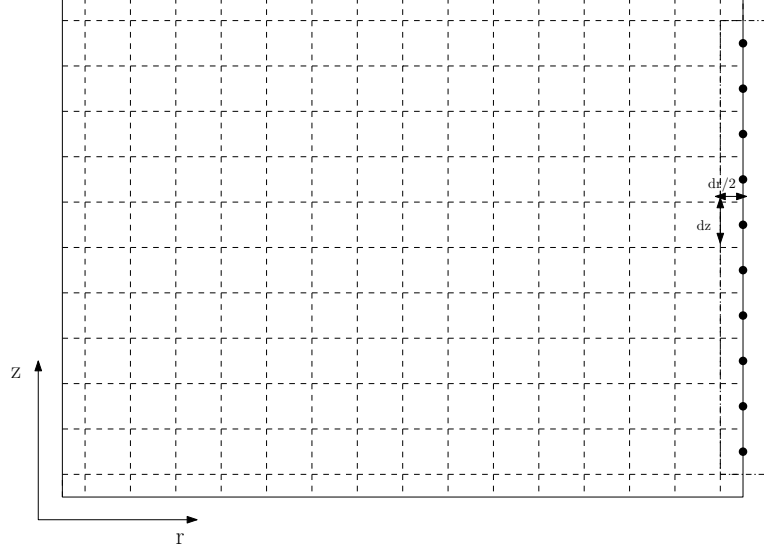- For a node at the outer boundary on lateral surface

Figure 3.4. Location of nodes on lateral surface

$$V_{cv} \quad = \quad 2\pi(m - \frac{1}{4})\Delta r(\frac{\Delta r}{2})\Delta z \qquad (3.22)$$

$$(\rho C_p)_e V_{cv}\left(\frac{T_{m,j}^{p+1} - T_{m,j}^p}{\Delta t}\right) \quad = \quad k2\pi(m - \frac{1}{2})\Delta r\Delta z\left(\frac{T_{m-1,j}^p - T_{m,j}^p}{\Delta r}\right)$$

$$+h2\pi m\Delta r\Delta z(T_f - T_{m,j}^p)$$

$$+k2\pi(m - \frac{1}{4})\Delta r(\frac{\Delta r}{2})\left(\frac{T_{m,j+1}^p - T_{m,j}^p}{\Delta z}\right)$$

$$+k2\pi(m - \frac{1}{4})\Delta r(\frac{\Delta r}{2})\left(\frac{T_{m,j-1}^p - T_{m,j}^p}{\Delta z}\right)$$
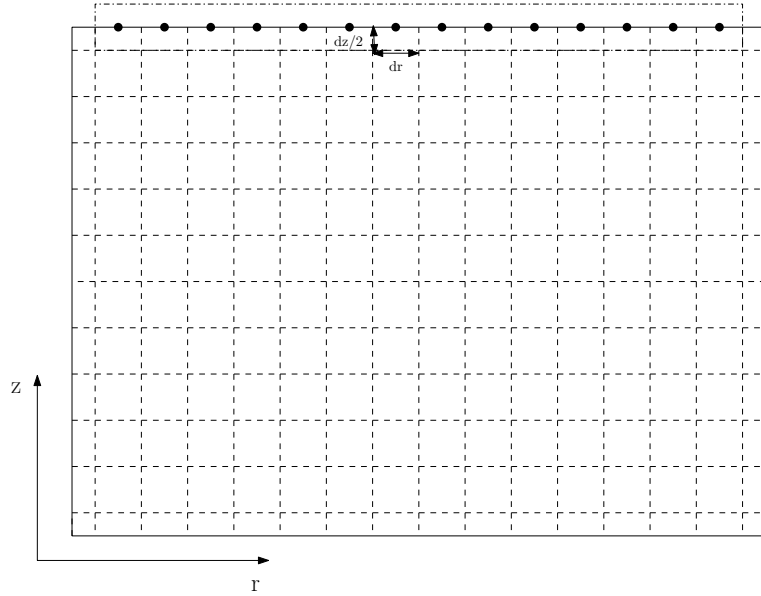
$$+\dot{q}V_{cv} \qquad (3.23)$$

- For a node at the interior of top

Figure 3.5. Location of interior nodes of top surface

$$V_{cv} = 2\pi i (\Delta r)^2 \frac{\Delta z}{2} \tag{3.24}$$

$$(\rho C_p)_e V_{cv} \left(\frac{T_{i,n}^{p+1} - T_{i,n}^p}{\Delta t} \right) = k 2\pi (i - \frac{1}{2}) \Delta r \frac{\Delta z}{2} \left(\frac{T_{i-1,n}^p - T_{i,n}^p}{\Delta r} \right)$$

$$+ k 2\pi (i + \frac{1}{2}) \Delta r \frac{\Delta z}{2} \left(\frac{T_{i+1,n}^p - T_{i,n}^p}{\Delta r} \right)$$

$$+ h 2\pi i (\Delta r)^2 (T_f - T_{i,n}^p)$$

$$+ k 2\pi i (\Delta r)^2 \left(\frac{T_{i,n-1}^p - T_{i,n}^p}{\Delta z} \right)$$

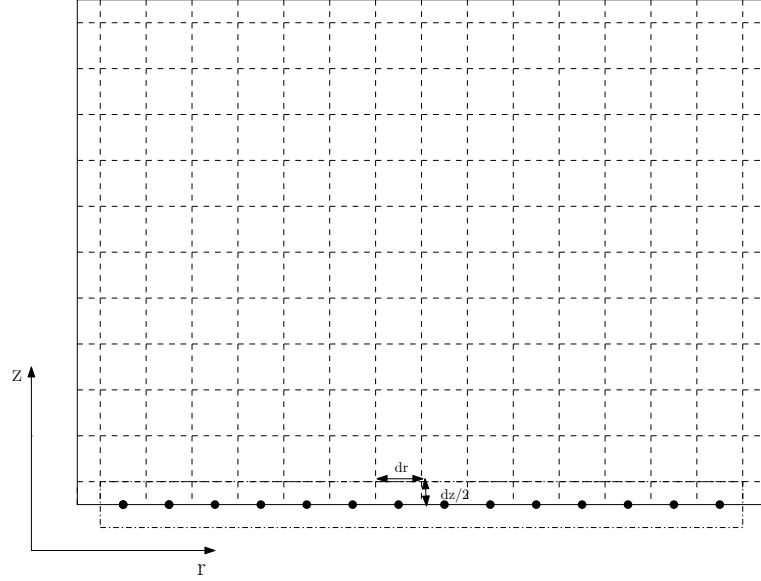$$+ \dot{q} V_{cv} \tag{3.25}$$

● For a node at the interior of bottom

Figure 3.6. Location of interior nodes of bottom surface

$$V_{cv} = 2\pi i (\Delta r)^2 \frac{\Delta z}{2} \tag{3.26}$$

$$(\rho C_p)_e V_{cv} \left(\frac{T_{i,1}^{p+1} - T_{i,1}^p}{\Delta t} \right) = k2\pi (i - \frac{1}{2}) \Delta r \frac{\Delta z}{2} \left(\frac{T_{i-1,1}^p - T_{i,1}^p}{\Delta r} \right)$$

$$+ k2\pi (i + \frac{1}{2}) \Delta r \frac{\Delta z}{2} \left(\frac{T_{i+1,1}^p - T_{i,1}^p}{\Delta r} \right)$$

$$+ h2\pi i (\Delta r)^2 (T_f - T_{i,1}^p)$$

$$+ k2\pi i (\Delta r)^2 \left(\frac{T_{i,2}^p - T_{i,1}^p}{\Delta z} \right)$$

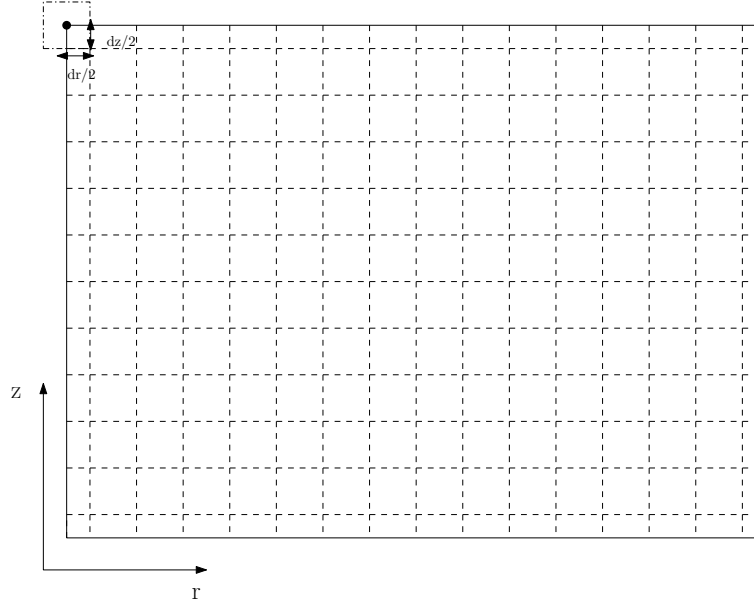$$+ \dot{q} V_{cv} \tag{3.27}$$

- For the node at the top center

Figure 3.7. Location of center node on top surface

$$V_{cv} \;=\; \pi \left(\frac{\Delta r}{2}\right)^2 \frac{\Delta z}{2} \tag{3.28}$$

$$(\rho C_p)_e V_{cv} \left(\frac{T_{1,n}^{p+1} - T_{1,n}^p}{\Delta t}\right) \;=\; k2\pi \frac{\Delta r}{2}\frac{\Delta z}{2}\left(\frac{T_{2,n}^p - T_{1,n}^p}{\Delta r}\right)$$

$$+ k\pi \left(\frac{\Delta r}{2}\right)^2 \left(\frac{T_{1,n-1}^p - T_{1,n}^p}{\Delta z}\right)$$

$$+ h\pi \left(\frac{\Delta r}{2}\right)^2 (T_f - T_{1,n}^p)$$

$$+ \dot{q}V_{cv} \tag{3.29}$$

- For the node at the bottom center

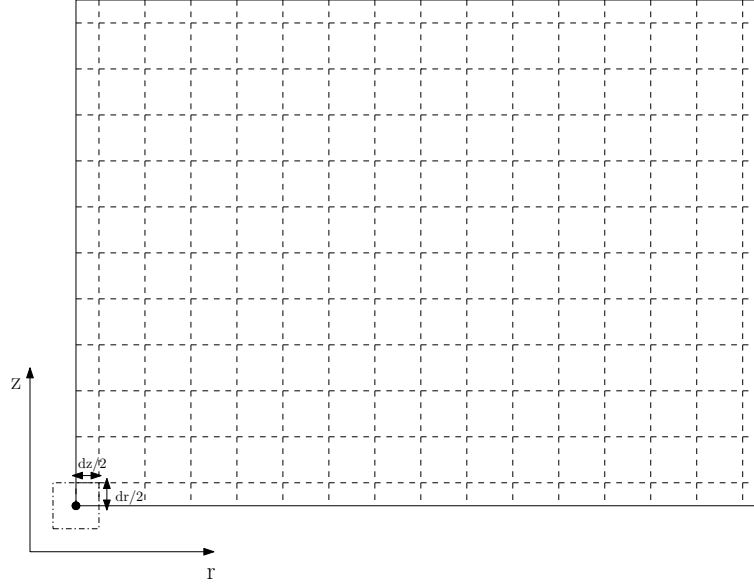Figure 3.8. Location of center node on bottom surface

$$V_{cv} = \pi \left(\frac{\Delta r}{2}\right)^2 \frac{\Delta z}{2} \qquad (3.30)$$

$$(\rho C_p)_e V_{cv} \left(\frac{T_{1,1}^{p+1} - T_{1,1}^p}{\Delta t}\right) = k2\pi \frac{\Delta r}{2} \frac{\Delta z}{2} \left(\frac{T_{2,1}^p - T_{1,1}^p}{\Delta r}\right)$$

$$+ k\pi \left(\frac{\Delta r}{2}\right)^2 \left(\frac{T_{1,2}^p - T_{1,1}^p}{\Delta z}\right)$$

$$+ h\pi \left(\frac{\Delta r}{2}\right)^2 (T_f - T_{1,1}^p)$$

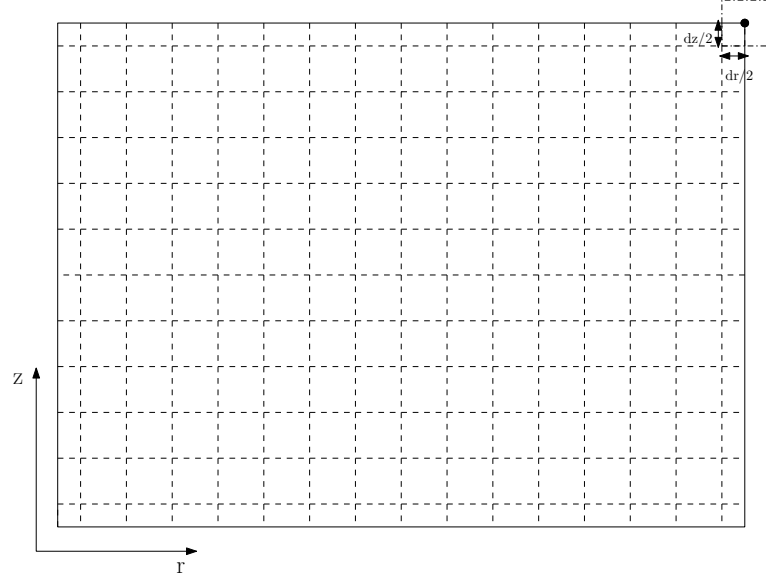$$+ \dot{q} V_{cv} \qquad (3.31)$$

- For the node at the top corner

Figure 3.9. Location of corner node on top surface

$$V_{cv} = 2\pi(m - \frac{1}{4})\Delta r \frac{\Delta r}{2}\frac{\Delta z}{2} \tag{3.32}$$

$$(\rho C_p)_e V_{cv}\left(\frac{T_{m,n}^{p+1} - T_{m,n}^p}{\Delta t}\right) = k2\pi(m - \frac{1}{2})\Delta r\left(\frac{\Delta z}{2}\right)\left(\frac{T_{m-1,n}^p - T_{m,n}^p}{\Delta r}\right)$$

$$+k2\pi(m - \frac{1}{4})\Delta r\left(\frac{\Delta r}{2}\right)\left(\frac{T_{m,n-1}^p - T_{m,n}^p}{\Delta z}\right)$$

$$+h2\pi m\Delta r\left(\frac{\Delta z}{2}\right)(T_f - T_{m,n}^p)$$

$$+h2\pi(m - \frac{1}{4})\Delta r\left(\frac{\Delta r}{2}\right)(T_f - T_{m,n}^p)$$

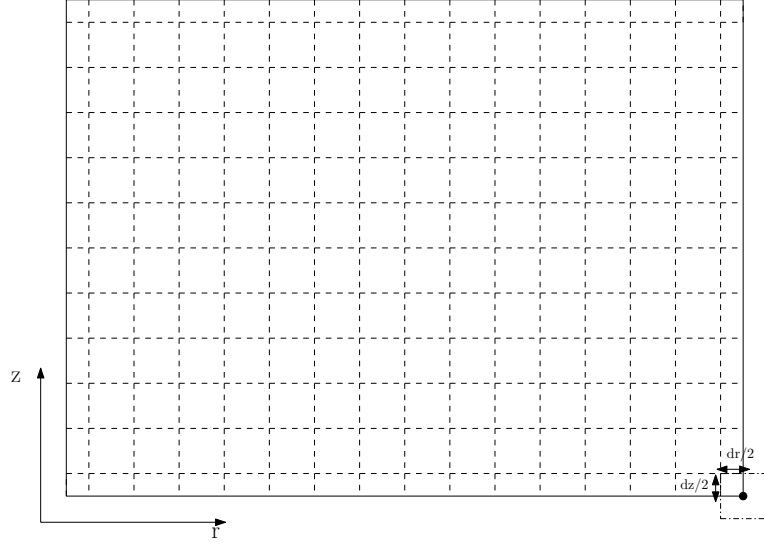$$+\dot{q}V_{cv} \tag{3.33}$$

- For the node at the bottom corner

Figure 3.10. Location of corner node on bottom surface

$$V_{cv} = 2\pi(m - \frac{1}{4})\Delta r \frac{\Delta r}{2} \frac{\Delta z}{2} \qquad (3.34)$$

$$(\rho C_p)_e V_{cv} \left(\frac{T_{m,1}^{p+1} - T_{m,1}^p}{\Delta t} \right) = k2\pi(m - \frac{1}{2})\Delta r \left(\frac{\Delta z}{2} \right) \left(\frac{T_{m-1,1}^p - T_{m,1}^p}{\Delta r} \right)$$

$$+ k2\pi(m - \frac{1}{4})\Delta r \left(\frac{\Delta r}{2} \right) \left(\frac{T_{m,2}^p - T_{m,1}^p}{\Delta z} \right)$$

$$+ h2\pi m \Delta r \left(\frac{\Delta z}{2} \right) (T_f - T_{m,1}^p)$$

$$+ h2\pi(m - \frac{1}{4})\Delta r \left(\frac{\Delta r}{2} \right) (T_f - T_{m,1}^p)$$

$$+ \dot{q} V_{cv} \qquad (3.35)$$

3.3.2. Stability Check for All Critical Nodes

Stability criterion requires that the multiplying term of $T_{i,j}^p$ should be always positive. In our energy balance equations there exists two terms which contain $T_{i,j}^p$. First one stems from the heat conducted and/or convected from the surrounding nodes to the central node, second comes from the heat generated as a result of kinetic reaction. Since the reaction is exothermic, second term is always positive. If Δt is selected such that first term is also positive, the stability of the explicit solution is provided in a rather conservative manner. Therefore for the stability check the positivity of the first term is ensured.

- For any interior node

$$
\left(
\begin{aligned}
& - \quad k2\pi(i - \frac{1}{2})\Delta z - k2\pi(i + \frac{1}{2})\Delta z \\
& - \quad k2\pi i\frac{(\Delta r)^2}{\Delta z} - k2\pi i\frac{(\Delta r)^2}{\Delta z} + (\rho C_p)_e 2\pi i(\Delta r)^2\frac{\Delta z}{\Delta t}
\end{aligned}
\right) > 0
$$

$$
\Delta t < \frac{(\rho C_p)_e i(\Delta r)^2\Delta z}{k(i - \frac{1}{2})\Delta z + k(i + \frac{1}{2})\Delta z + ki\frac{(\Delta r)^2}{\Delta z}} \tag{3.36}
$$

- For a node on the symmetry axis at $r = 0$ excluding the ones on the boundaries

$$
\left(
\begin{aligned}
& - \quad k\pi\Delta z - k\pi\left(\frac{\Delta r}{2}\right)^2\frac{1}{\Delta z} \\
& - \quad -k\pi\left(\frac{\Delta r}{2}\right)^2\frac{1}{\Delta z} + (\rho C_p)_e\pi\left(\frac{\Delta r}{2}\right)^2\frac{\Delta z}{\Delta t}
\end{aligned}
\right) > 0
$$

$$
\Delta t < \frac{(\rho C_p)_e\pi\left(\frac{\Delta r}{2}\right)^2\Delta z}{k\Delta z + k\left(\frac{\Delta r}{2}\right)^2\frac{2}{\Delta z}} \tag{3.37}
$$

- For a node at the outer boundary on lateral surface

$$\bigg(\quad - \quad k2\pi(m - \frac{1}{2})\Delta z - h2\pi m\Delta r\Delta z - k2\pi(m - \frac{1}{4})\Delta r\frac{\Delta r}{2}\frac{1}{\Delta z}$$
$$- \quad k2\pi(m - \frac{1}{4})\Delta r\frac{\Delta r}{2}\frac{1}{\Delta z} + (\rho C_p)_e 2\pi(m - \frac{1}{4})\Delta r\frac{\Delta r}{2}\frac{\Delta z}{\Delta t} \bigg) > 0$$

$$\Delta t < \frac{(\rho C_p)_e(m - \frac{1}{4})\Delta r\frac{\Delta r}{2}\Delta z}{k(m - \frac{1}{2})\Delta z + hm\Delta r\Delta z + k(m - \frac{1}{4})\Delta r\frac{\Delta r}{\Delta z}} \qquad (3.38)$$

- For a node at the interior of top

$$\bigg(\quad - \quad k\pi(i - \frac{1}{2})\Delta z - k\pi(i + \frac{1}{2})\Delta z - k2\pi i\Delta r\frac{\Delta r}{\Delta z}$$
$$+ \quad h2\pi i(\Delta r)^2 + (\rho C_p)_e\pi i(\Delta r)^2\frac{\Delta z}{\Delta t} \bigg) > 0$$

$$\Delta t < \frac{(\rho C_p)_e i(\Delta r)^2\Delta z}{k(i - \frac{1}{2})\Delta z + k(i + \frac{1}{2})\Delta z + h2i(\Delta r)^2 + k2i\frac{(\Delta r)^2}{\Delta z}} \qquad (3.39)$$

- For a node at the interior of bottom

$$\bigg(\quad - \quad k\pi(i - \frac{1}{2})\Delta z - k\pi(i + \frac{1}{2})\Delta z - k2\pi i\Delta r\frac{\Delta r}{\Delta z}$$
$$+ \quad h2\pi i(\Delta r)^2 + (\rho C_p)_e\pi i(\Delta r)^2\frac{\Delta z}{\Delta t} \bigg) > 0$$

$$\Delta t < \frac{(\rho C_p)_e i(\Delta r)^2\Delta z}{k(i - \frac{1}{2})\Delta z + k(i + \frac{1}{2})\Delta z + h2i(\Delta r)^2 + k2i\frac{(\Delta r)^2}{\Delta z}} \qquad (3.40)$$

- For the node at the top center

$$\left(-k\pi\frac{\Delta z}{2} - k\pi(\frac{\Delta r}{2})^2\frac{1}{\Delta z} + h\pi(\frac{\Delta r}{2})^2 + (\rho C_p)_e\pi(\frac{\Delta r}{2})^2\frac{\Delta z}{2\Delta t} \right) > 0$$

$$\Delta t < \frac{(\rho C_p)_e(\Delta r)^2\Delta z}{2(2k\Delta z + k\frac{(\Delta r)^2}{\Delta z} + h(\Delta r)^2)} \tag{3.41}$$

- For the node at the bottom center

$$\left(-k\pi\frac{\Delta z}{2} - k\pi(\frac{\Delta r}{2})^2\frac{1}{\Delta z} + h\pi(\frac{\Delta r}{2})^2 + (\rho C_p)_e\pi(\frac{\Delta r}{2})^2\frac{\Delta z}{2\Delta t} \right) > 0$$

$$\Delta t < \frac{(\rho C_p)_e(\Delta r)^2\Delta z}{2(2k\Delta z + k\frac{(\Delta r)^2}{\Delta z} + h(\Delta r)^2)} \tag{3.42}$$

- For the node at the top corner

$$\left(\begin{aligned} &- k\pi(m-\frac{1}{2})\Delta z - k\pi(m-\frac{1}{4})\Delta r\frac{\Delta r}{\Delta z} - h\pi m\Delta r\Delta z \\ &+ h\pi(m-\frac{1}{4})\Delta r\Delta r + (\rho C_p)_e\pi(m-\frac{1}{4})(\Delta r)^2\frac{\Delta z}{2\Delta t} \end{aligned} \right) > 0$$

$$\Delta t < \frac{(\rho C_p)_e(m-\frac{1}{4})(\Delta r)^2\Delta z}{2(k(m-\frac{1}{2})\Delta z + k(m-\frac{1}{4})\frac{(\Delta r)^2}{\Delta z} + hm\Delta r\Delta z + h(m-\frac{1}{4})(\Delta r)^2)} \tag{3.43}$$

- For the node at the bottom corner

$$
\begin{aligned}
\Big(\quad - \quad & k\pi(m - \tfrac{1}{2})\Delta z - k\pi(m - \tfrac{1}{4})\Delta r\frac{\Delta r}{\Delta z} - h\pi m\Delta r\Delta z \\
+ \quad & h\pi(m - \tfrac{1}{4})\Delta r\Delta r + (\rho C_p)_e\pi(m - \tfrac{1}{4})(\Delta r)^2\frac{\Delta z}{2\Delta t} \Big) > 0
\end{aligned}
$$

$$
\Delta t < \frac{(\rho C_p)_e(m - \tfrac{1}{4})(\Delta r)^2\Delta z}{2(k(m - \tfrac{1}{2})\Delta z + k(m - \tfrac{1}{4})\frac{(\Delta r)^2}{\Delta z} + hm\Delta r\Delta z + h(m - \tfrac{1}{4})(\Delta r)^2)} \tag{3.44}
$$

4. RESULTS

The energy balance equations derived for each node are solved numerically with explicit scheme using MATLAB. In the code the geometric parameters and the thermophysical properties of materials can be specified with respect to experimental setups or previous numerical studies. Also the number of nodes in each direction can be defined by the user. Before evaluating the temperature distribution, the code runs a function to investigate the optimum Δt that satisfies the stability criteria for the specified combination of reactor geometry, number of nodes and properties of the materials.

For the base case reactor geometry is assumed to be similar to the geometry of the conventional metal hydride tanks. Therefore the radial length and the longitudinal length are specified as 0.05 m and 0.10 m, respectively. The thermophysical properties of hydrogen and metal are listed in Table 4.1.

Table 4.1. Thermophysical Properties of Materials at Atmospheric Pressure and at Room Temperature

Property	Metal($LaNi_5$)	Hydrogen(H_2)
Density,ρ ($kg\ m^{-3}$)	8400	0.0838
Porosity,ε	0.5	–
Molecular weight,($kg\ kmol^{-1}$)	432.4	2
Specific Heat,C_p ($J\ kg^{-1}\ K^{-1}$)	419	14890
Thermal Conductivity,k ($W\ m^{-1}\ K^{-1}$)	2.4	0.24
Heat of Formation, ΔH^0 ($Wm^{-1}K^{-1}$)	$-1.545\mathrm{x}10^7$	–

Effective thermal conductivity is calculated from Equation 3.3 by using the relevant values. The parameters related to reaction bed and reaction are listed in Table 4.2.

Table 4.2. Data Used in Numerical Analysis

Saturated density of $LaNi_5$, ρ_{ss} (kg m^{-3})	8527
Heat Transfer Coefficient,h ($W\ m^{-2}\ K^{-1}$)	1652
Initial Bed Temp., T_i (K)	293
Cooling Fluid Temp., T_∞ (K)	293
Inlet Hydrogen Pressure, P (bar)	10

For the base case the Δt is found to be 0.5273 s. The code is run until the whole metal bed is reached to the initial temperature by cooling. This is approximately 12000 s in real time. So the program does the calculations for 22758 time steps.

Numerical simulation results present instantaneous the temperature and density distribution during absorption process for the specified parameters, given in Figure 4.1 and Figure 4.2 respectively. One of the characteristics of hydriding process in intermetallic compounds is the sudden increase of temperature in hydride bed. This is due to release of high quantities of energy per time during exothermic reaction. Dramatic temperature gradients are observed within the first 500 s of the absorption. The difference in temperature distribution throughout the hydride bed is dissipated in time by the help of convecting fluid. This sequence is summarized in Figure 4.1.
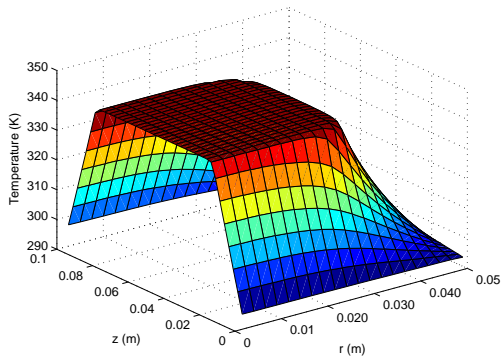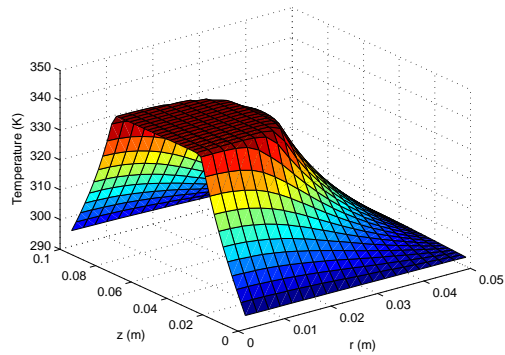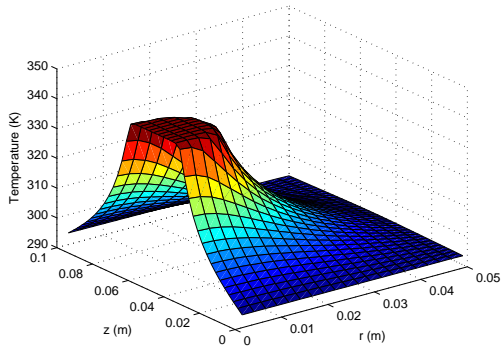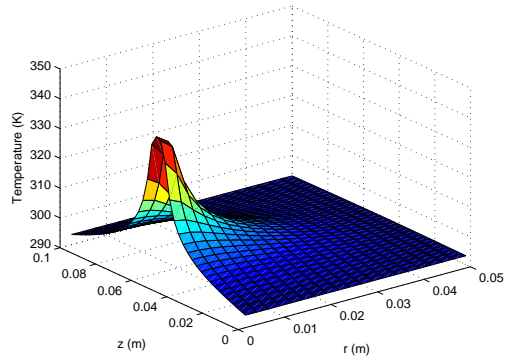
(a) at $t = 3000s$

(b) at $t = 6000s$

(c) at $t = 9000s$

(d) at $t = 10500s$

Figure 4.1. Temperature distribution in reactor at selected times
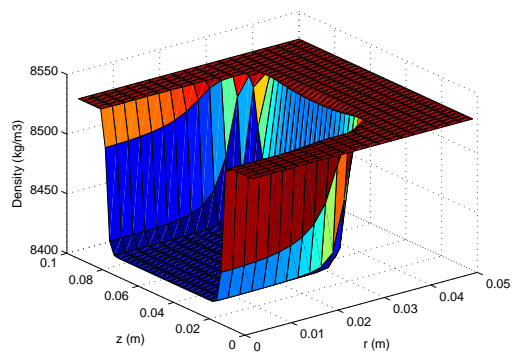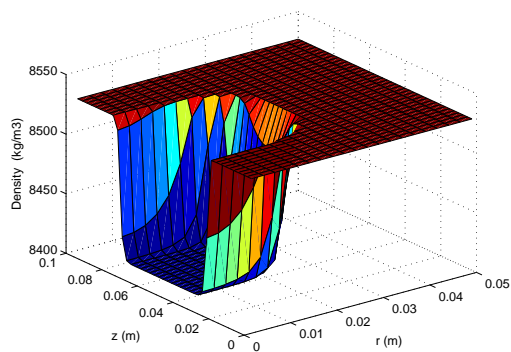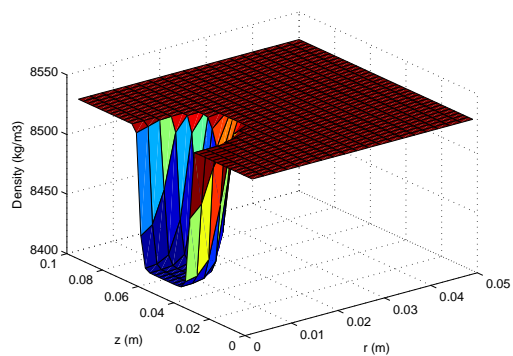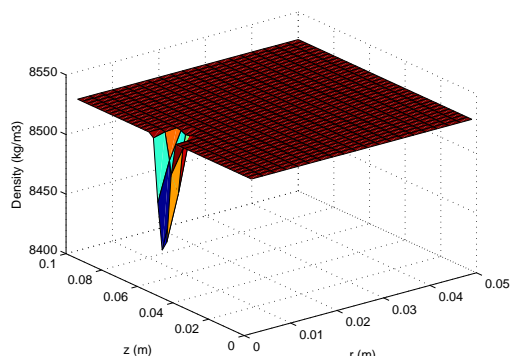
(a) at $t = 3000s$

(b) at $t = 6000s$

(c) at $t = 9000s$

(d) at $t = 10500s$

Figure 4.2. Density profile in the reactor at selected times

The total mass of the absorbed hydrogen is evaluated with respect to total mass of the metal bed. The studies of Sandrock reveals that maximum H-capacity of LaNi$_5$ is 1.49 wt.% (14.90 g/kg alloy)[7]. For the chosen base case the alloy weights 3.2986 kg. Namely maximum hydrogen that can be absorbed for the specified geometry and the combination of the given boundary and initial conditions is 0.0491 kg. The numerical results can be seen in Figure 4.3.They show good correlation with the previous numerical and experimental studies [12, 26].
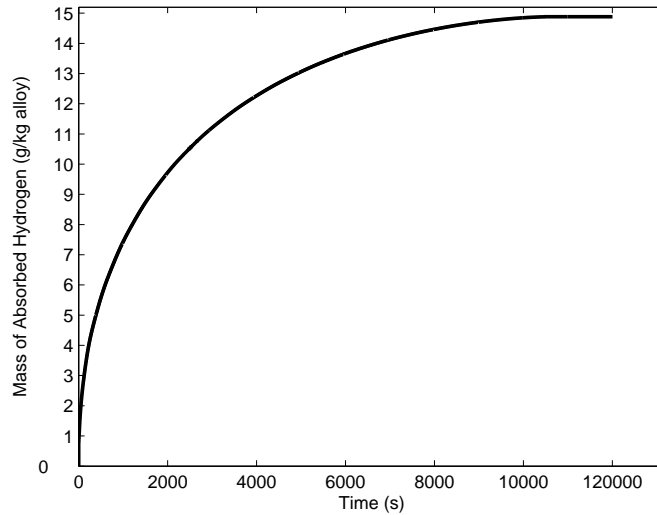

Figure 4.3. Total mass of hydrogen absorbed per kg alloy

Figure 4.4 shows the temperature evaluation within the reactor at three points. Since the origin is chosen to be the left bottom corner on the symmetry axis, these points lay in the middle of the one half of the metal-hydride bed and their altitude differ by 0.025 m. The point which is near the inlet experiences slightly higher temperature values with respect to the point which is near the bottom. Whereas the point in the middle preserves the high temperature during hydriding. This is reasonable due to the fact that the points in the upper portion of the reactor meet the compressed hydrogen earlier thereby they experience the sequence of hydriding, temperature increase and temperature decrease earlier than the points situated at relatively lower locations. Also it is seen that the point in the middle preserves the high temperature during hydriding since the removal of heat from the center points of the reactor takes longer.
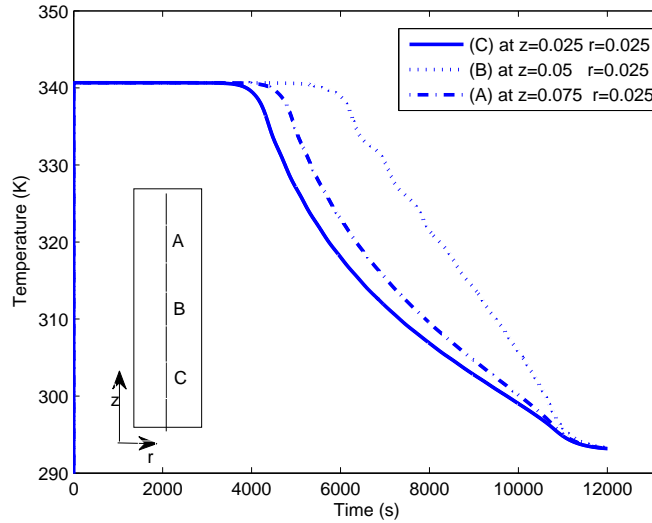
Figure 4.4. Temperature evaluation at different locations

4.1. Effect of H/R ratio

In order to study the effect of geometric factors, various cases are examined. The reactor volume is kept constant whereas radial and longitudinal lengths are changed accordingly. The thermophysical properties and the boundary conditions are maintained the same as the ones in the base case. Also the number of nodes in each direction is preserved.

Since the optimum Δt that satisfies the stability criterion is a function of reactor geometry, Δt value and thereby the number of time steps to be evaluated are different for each case. Δt decreases as the ratio of longitudinal length (height) to radial length (radius) increases. Table 4.3 summarizes the seven different cases that are studied. The term $Final\ t$ is used to specify the time needed for the reactor to reach this saturation level.

Table 4.3. Comparison of Different Reactor Geometries

H/R	Radius(m)	Height(m)	Absorbed Mass (kg)	Final t (s)
1/2	0.0794	0.0397	0.0489	3834
1	0.0630	0.0630	0.0489	7770
2	0.05	0.1	0.0489	10190
3	0.0437	0.1310	0.0489	9435
4	0.0397	0.1587	0.0489	8215
5	0.0368	0.1842	0.0489	7170
10	0.0292	0.2924	0.0489	4565

During absorption of same amount of hydrogen, the heat removed from lateral, top and bottom surfaces are listed in Table 4.4.

Table 4.4. Comparison of Heat Removed for Same Amount of Hydrogen Absorption

H/R	Absorbed Mass (kg)	Q_{lat}(MJ)	Q_{tb}(MJ)	Q_{total} (MJ)
1/2	0.0489	0.1725	0.9650	1.1375
1	0.0489	0.5701	0.7662	1.3363
2	0.0489	1.0390	0.3719	1.4109
3	0.0489	1.3273	0.2455	1.5729
4	0.0489	1.4764	0.1812	1.6576
5	0.0489	1.5590	0.1432	1.7021
10	0.0489	1.7396	0.0727	1.8123

In Figure 4.5 the total heat removed for the same amount of hydrogen to be absorbed is compared. In Figure 4.6 the effect of reactor geometry on saturation time is graphed, where final time indicates the time needed to reach the predefined saturation level. It is seen that for H/R equals to 2 the time needed to reach saturation experiences a maximum. However as H/R is increased further the time to reach saturation decreases. This is due to the fact that lateral surface is more effective in cooling process of the metal-hydride reactors. Therefore as the area of lateral surface increases, the resistance for heat transfer decreases which results in decrease in time needed for saturation.
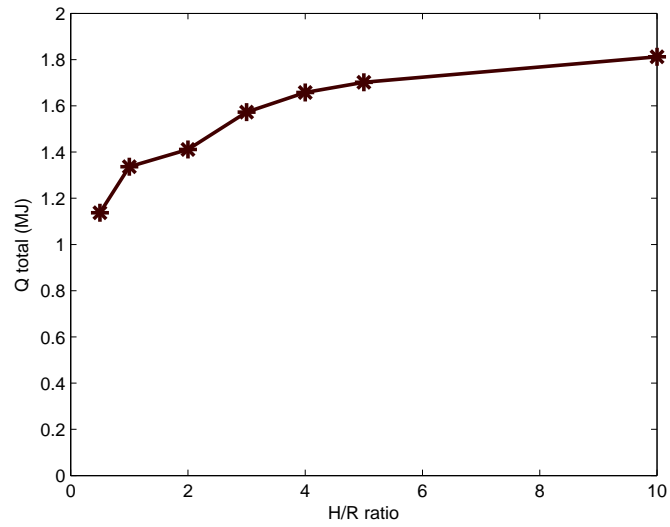
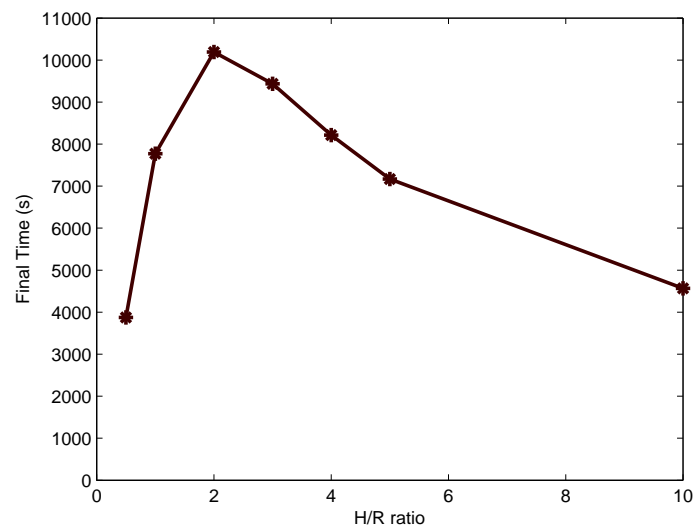Figure 4.5. Comparison of different H/R values on total heat removed

Figure 4.6. Comparison of different H/R values on saturation time

Moreover as H/R value increases from 1 to 3, a decrease in the total mass of absorbed hydrogen is observed. As can be seen in Figure 4.7 ratio of mass absorbed by metal alloy states a minimum for the values of H/R between 2 and 3. This can be explained such that; within this range the increased resistance to heat transfer along z axis results in heat transfer being highly dependent on z direction. Whereas above $H/R = 3$ the absorbed mass of hydrogen increases as the length of reactor increases which shows that the trend of the problem changes. The decrease in resistance along r direction is more dominant. Therefore above this range the heat transfer is dependent on r direction. For very large and very small values of H/R the problem can be considered to be one dimensional. However for intermediate values it should be considered to be two dimensional. This correlation is also seen in the previous studies [12].
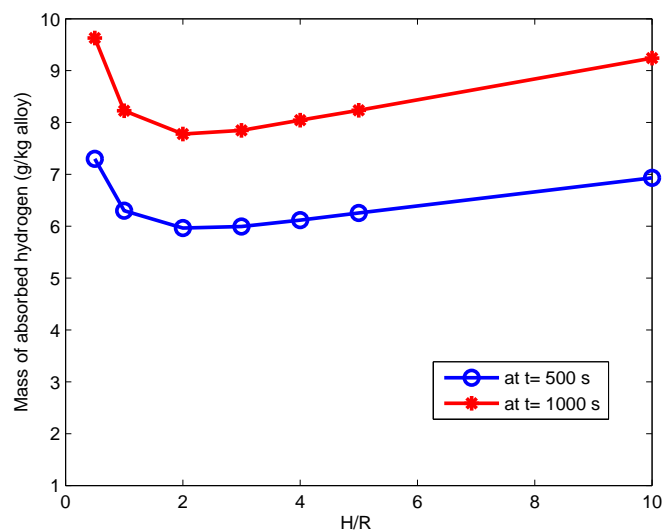

Figure 4.7. Effect of H/R on mass of absorbed hydrogen at selected times

It is obvious that reactor geometry affects the temperature distribution and the instantaneous density evolution within the reactor. Figure 4.8 illustrates the specified parameters evaluated at 4000s for selected reactors which are equal in volume but different in height and radius. As the ratio of height to radius of the reactor increases, the lateral surface becomes more effective in cooling.
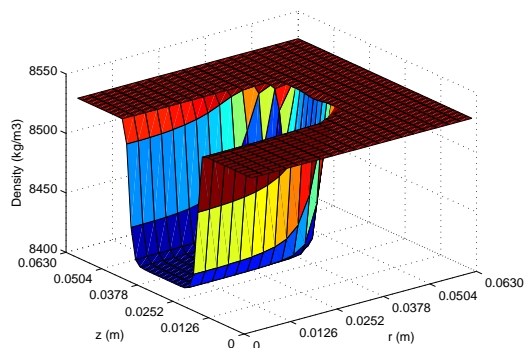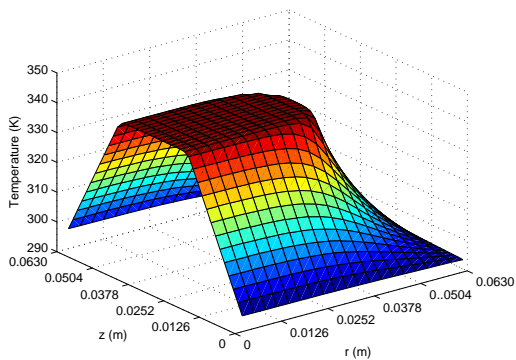
a)For $H/R = 1$
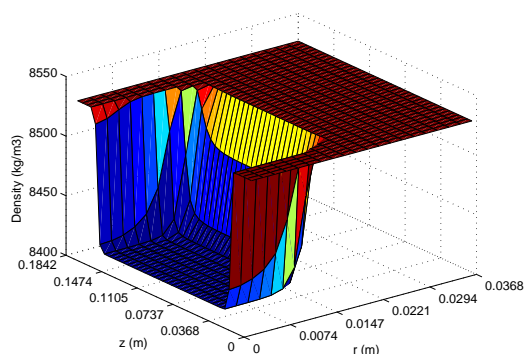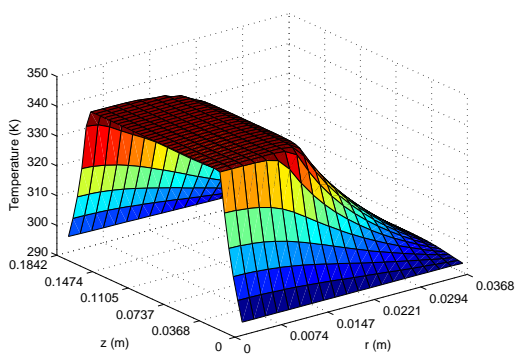
b)For $H/R = 5$

c)For $H/R = 10$

Figure 4.8. Temperature and density distributions at 4000 s for different H/R

4.2. Effect of Inlet Hydrogen Pressure

Inlet hydrogen pressure is one of the most influential parameters in hydriding reaction. This is investigated for the three possible and mostly employed 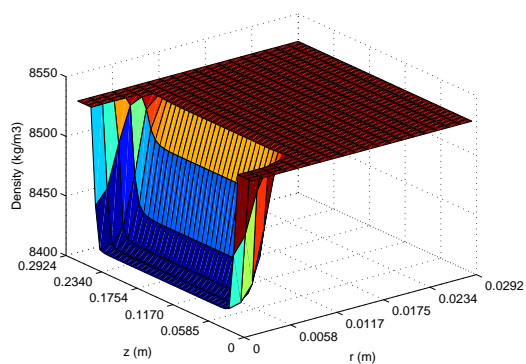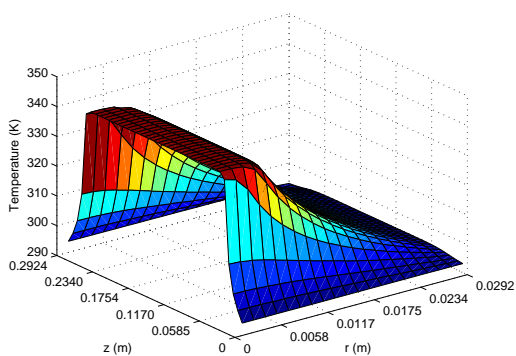pressure values: 5 bar, 10 bar (also the base case), 15 bar. As in section 4.1, all the other parameters are kept constant for the numerical analysis.

Table 4.5. Comparison of Different Inlet Hydrogen Pressure

Pressure (bar)	Absorbed Mass (kg)	Final t (s)	Max Temperature (K)
5	0.0491	17190	319.88
10	0.0489	10190	340.65
15	0.0487	7995	354.11

Increase in the inlet hydrogen pressure results in the acceleration of the absorption reaction. This leads to an increase in heat released per time. Therefore higher maximum temperature is observed when the inlet pressure is 10 or 15 bars. On the other hand since the reaction kinetics is faster in higher inlet pressure case, the time needed for the hydride bed to reach saturation is much less. This is shown in Figure 4.9. When 15 bar case is compared with 5 bar case, less than half of the time needed in the latter case is enough for reaching saturation in former case. However the cost of this quick hydriding is a problem for removing larger heat quantities per time.
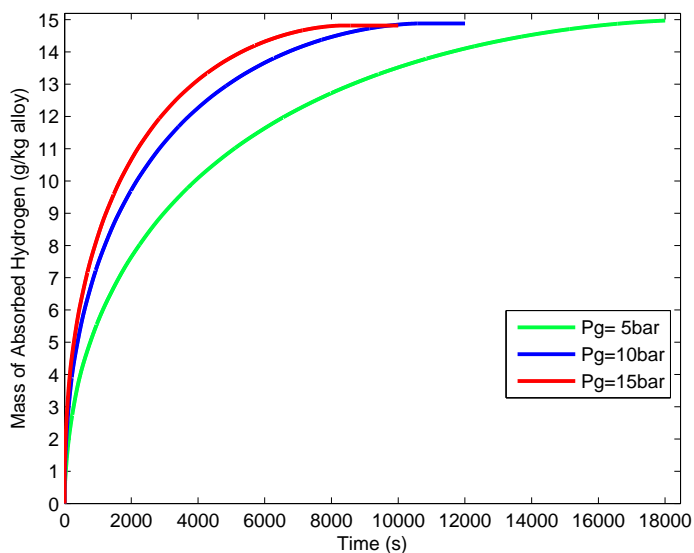
Figure 4.9. Comparison of different inlet pressures on saturation time

In Figure 4.10 the effect of inlet hydrogen pressure on temperature evaluation is graphed. The heating and cooling tendency of the metal hydride bed is inspected at a node in the middle of the hydride bed which has coordinates $z = 0.05$ m and $r = 0.025$ m. As explained in Figure 4.4 this is the point where the removal of the released heat continues longer than at other points. Figure 4.10 is correlated with the experimental studies.[22]

Figure 4.10. Comparison of different inlet pressures on temperature evaluation at

z=0.05 r=0.025

4.3. Effect of Metal Porosity

The methods used to obtain $LaNi_5$ powders and the activation process of the alloy, which is basically charging the reactor at constant temperature and pressure and discharging for various number of cycles, result in different particle diameters. Therefore the previous experimental studies show variations at particle size and porosity. In this study also the effect of metal-hydride bed is considered.
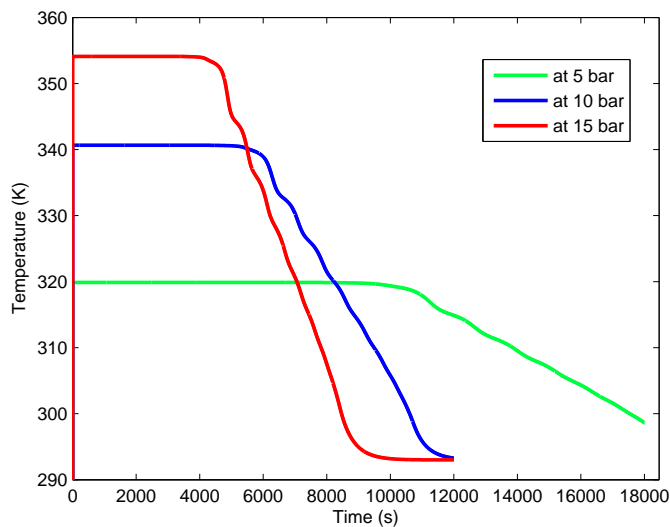
It is obvious that for the same volume the hydrogen mass absorbed will be much more in the reactor where the porosity is less. As stated in Equation 3.3, effective thermal conductivity is a function of porosity. Also Δt calculated with respect to the stability criterion is a function of effective thermal conductivity. As a result the change in porosity effects the calculated values for effective thermal conductivity of the metal-hydride bed and the computational time steps. The maximum temperature experienced during hydriding is same for all three cases that is 340 K.

Table 4.6. Comparison of Different Metal Porosity

Porosity	Absorbed Mass (kg)	Abs. Mass (g/ kg alloy)	k_e ($W\ m^{-1}\ K^{-1}$)	Final t (s)
0.5	0.0489	14.8241	1.32	10190
0.6	0.0391	14.8165	1.104	9726
0.7	0.0293	14.8039	0.888	8996

For comparison the volume of the reactor, the inlet hydrogen pressure, the initial temperatures are constant in all three cases. Figure 4.11 shows that maximum weight percent of mass absorbed by the alloy is quite identical for both three cases. The maximum temperature experienced during hydriding is same for all three cases that is 340 K. This also shows the consistency achieved in numerical analysis.

(a) For $\varepsilon = 0.6$ (b) For $\varepsilon = 0.7$
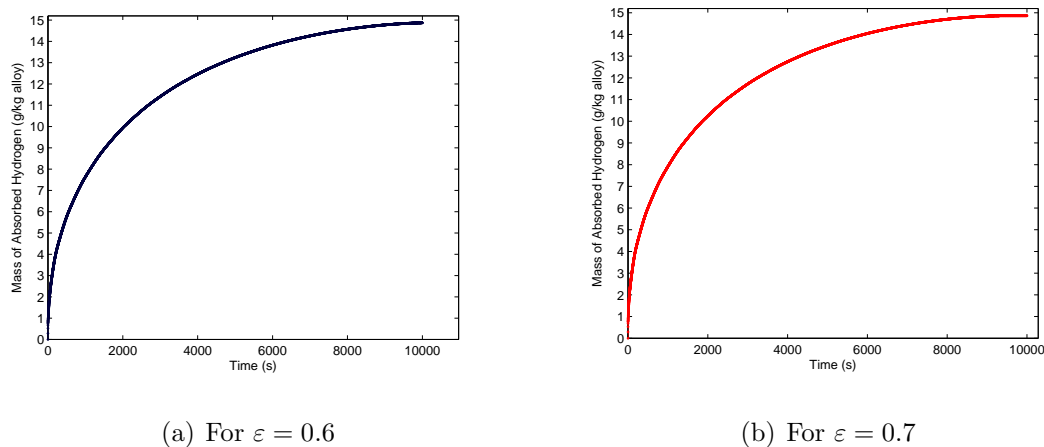
Figure 4.11. Total mass absorbed per kg alloy with different porosity

4.4. Effect of Initial Metal Bed Temperature

Conventional metal-hydride tanks are mostly filled at outdoor spaces therefore the effect of initial temperature of the tank is investigated. As in Section 4.1 only the inspected parameter is changed with keeping the others constant. Therefore maximum mass of absorbed hydrogen, maximum temperature experienced, thermophysical properties of the metal alloy are same as in the base case. As can be seen in Figure 4.12 time needed to reach saturation is slightly less for cases with low initial temperature.

Figure 4.12. Comparison of different initial bed temperatures on saturation time

4.5. Effect of Cooling Fluid Temperature

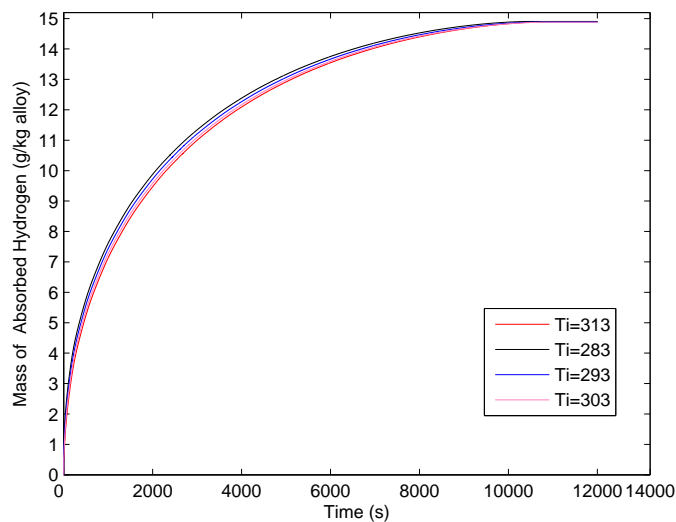Variety in cooling options is noticed for conventional systems. Besides the design of the reactor with fins or cooling channels, the temperature of the cooling fluid is seen to have a dramatic effect on saturation time. Three cases are studied which are given in Table 4.7.

Table 4.7. Comparison of Different Cooling Fluid Temperature

T_f (K)	Absorbed Mass (kg)	Final t (s)
293	0.0489	10190
298	0.0489	11330
303	0.0489	12774

For the defined base case under these conditions an increase in cooling fluid temperature by 10K leads to an increase in saturation time of approximately 45 minutes. This corresponds to an increase of 25 % in filling time of the metal-hydride tank. This dramatic rise stems from the fact that as the temperature of the cooling fluid increases the rate of removal of heat from the bed decreases which also means a decrease in reaction rate.
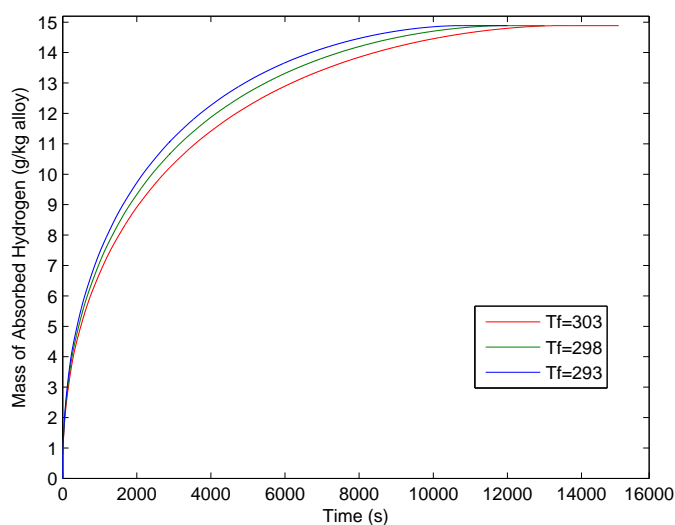

Figure 4.13. Comparison of different cooling fluid temperatures on saturation time

5. CONCLUSIONS

In this study heat and mass transfer processes through absorption of hydrogen in LaNi$_5$ intermetallic compound is investigated. The governing equations which describe reaction kinetics of hydriding is obtained from the previous studies. These are embedded in mass transfer equations. Due to the physics of the problem the mass and the heat transfer equations are solved simultaneously. Local thermal equilibrium approach is adopted in transient heat conduction with convective boundary conditions. Energy balance method is used to discretize the coupled equations in finite difference explicit scheme. For the chosen geometry nine critical locations are confirmed. The stability check is done based on discretization equations that are derived for each node.

For the numerical analysis, different than the previous studies a code in MAT-LAB is developed based on explicit formulation. Numerical simulations showed good correlations with the experimental data given in literature and with the previous studies.

A base case which has similar geometry to the conventional metal-hydride tanks is studied. The effects of reactor geometry, inlet hydrogen pressure, porosity of the metal alloy, initial bed temperature and cooling fluid temperature are investigated.

For our case it is seen that as the height to radius ratio of the reactor bed is changed, the time needed for the metal to reach saturation changes significantly. In general, less time is needed to reach saturation for geometries where H/R is larger. Also it is demonstrated that instantaneous absorbed mass of hydrogen is smallest when H/R is between 2 to 3. For this interval the absorption rate seems to decrease due to the reduction in removal of heat released during hydriding from the medium.

Inlet hydrogen pressure is found to be one of the most important parameter during hydriding. For the same geometry, under the same initial and boundary conditions the hydriding time of reactor with inlet pressure of 5 bar is more than twice the time

needed for the reactor with inlet pressure of 15 bar.

The metal-hydride bed porosity directly affects the effective thermal conductivity. Increasing porosity results in decreasing effective thermal conductivity, decreasing increments for time steps thereby increasing the run times for analysis. Nevertheless the maximum weight percent of hydrogen that can be absorbed to metal alloy is constant for all cases.

Initial bed temperature of the alloy slightly affects the time needed to reach saturation. Whereas it is observed that the temperature of the cooling fluid has a significant effect on this aspect. Cooling fluid is critical in removal of heat generated during exothermic absorption process and in order to achieve high absorption rate this heat should be conducted and convected as quickly as possible. This prominent effect is shown in simulations such that; 10 K increase in cooling fluid temperature results in an increase of 25 percent of time needed to reach saturation.

6. FUTURE WORK

- Desorption characteristics of LaNi$_5$ can be evaluated by applying appropriate changes in simulation related to reaction kinetics and energy balance equations.
- Thermophysical properties of the metal are temperature dependent. The changes in thermophysical properties can be inserted in the analysis.
- Dynamic sorption characteristics are effecting the A and B constants in Van't Hoff equation. If H/M is evaluated with respect to temperature distribution over the metal hydride, the changes in A and B can be calculated, the effect of dynamic sorption characteristics can be investigated through the calculated equilibrium pressure.

REFERENCES

1. Balat, M., *Potential Importance of Hydrogen as a Future Solution to Environmantal and Transportation Problems*, International Journal of Hydrogen Energy, Vol. 33, pp. 4018-4029, 2008.

2. Zhang, J., T. S. Fisher, P. V. Ramachandran, J. P. Gore, I. Mudawar, *A Review of Heat Transfer Issues in Hydrogen Storage Technologies*, Journal of Heat Transfer, Vol. 127, pp. 1391-1399, 2005.

3. Schimmel, H. G., 2004, Towards a Hydrogen Driven Society? Calculations and Neutron Scattering on Potential Hydrogen Storage Materials, M.S. Thesis, Delft University.

4. BP. British Petrol; Hydrogen for transport. http://www.bp.com 2006.

5. Sakintuna, B., F. L. Darkim, and M. Hirscher, *Metal Hydride for Solid Hydrogen Storage: A Review*, International Journal of Hydrogen Energy, Vol. 32, pp. 1121-1140, 2007.

6. U.S. Department of Energy, Office of Hydrogen, Fuel Cells, and Infrastructure Technologies, 2009, Multi-Year Research, Development and Demonstration Plan, http://www1.eere.energy.gov/hydrogenandfuelcells/mypp/

7. Sandrock, G., *A Panoramic Overview of Hydrogen Storage Alloys From a Gas Reaction Ponit of View*, Journal of Alloys and Compounds, 293-295, pp. 877-888, 1999.

8. Wagemans, R.W.P., 2006, Magnesium for Hydrogen Storage : from Micrometer to Nanometer, Ph.D. Thesis, Utrecht University.

9. Dantzer, P., *Properties of Intermetallic Compounds Suitable for Hydrogen Storage*

Applications, Materials Science and Engineering A329-331, pp.313-320, 2002.

10. Lucas, G.G. and W.L. Richards, *Mathematical Modelling Of Hydogen Storage Systems*, International Journal of Hydrogen Energy, Vol. 9, pp. 225-231, 1984.

11. Mayer, U., M. Groll and W. Supper, *Heat and Mass Transfer in Metal Hydride Reaction Beds*, Journal of Less-Common Metals, Vol. 131, pp. 235-244, 1987.

12. Jemni, A. and S.B. Nasrallah, *Study of Two Dimensonal Heat and Mass Transfer During Absoption in a Metal-Hydrogen Reactor*, International Journal of Hydrogen Energy, Vol. 20, pp. 43-52, 1995.

13. Patankar, S. V., *Numerical Heat Transfer and Fluid Flow*, Hemisphere Publication Cooperation, 1980.

14. Whitaker, S., *Simultaneous Heat, Mass and Momentum Transfer in Porous Media: A Theory of Drying*, Advances in Heat Transfer, Vol. 13, Academic Press, 1977.

15. Jemni, A. and S.B. Nasrallah, *Heat and Mass Transfer Models In Metal Hydride Reactor*, International Journal of Hydrogen Energy, Vol. 22, No.1, pp. 67-76, 1997.

16. Nakagawa, T., A. Inomata, H. Aoki and T. Miura, *Numerical Analysis of Heat and Mass Transfer Characteristics in the Metal Hydride Bed*, International Journal of Hydrogen Energy, Vol. 25, pp. 339-350, 2000.

17. Inomata, A., H. Aoki and T. Miura, *Measurement and Modelling of Hydriding and Dehyriding Kinetics*, Journal of Alloys and Compounds, Vol. 278, pp. 103-109, 1998.

18. Mat, M. D. and Y. Kaplan, *Numerical Study of Hydrogen Storage in an Lm-Ni5 Hydride Reactor*, International Journal of Hydrogen Energy, Vol. 26, pp. 957-963, 2001.

19. Aldas, K., M. D. Mat and Y. Kaplan, *A Three-Dimensional Mathematical Model for Absorption in a Metal hydride Bed*, International Journal of Hydrogen Energy,

Vol. 27, pp. 1049-1056, 2002.

20. Demircan, A., M. Demiralp, Y. Kaplan, M. D. Mat and T.N. Veziroglu, *Experimental and Theoretical Analysis of Hydrogen Absorption in LaNi5-H2 Reactors*, International Journal of Hydrogen Energy, Vol. 30, pp. 1437-1446, 2005.

21. Kikkinidesa, E. S., M. C. Georgiadisb and A. K. Stubose, *Dynamic Modelling and Optimization of Hydrogen Storage in Metal Hydride Beds*, Energy, Vol. 31, pp. 2428-2446, 2006.

22. Kaplan, Y., M. D. Mat, B. Ibrahimoglu, N. Veziroglu, R. Alibeyli and S. Kuliyev, *Heat and Mass Transfer of Hydrogen Storage in Metal-Hydrogen Reactors*, WHEC 2006, Lyon France, 2006.

23. Askri, F., A. Jemni and S.B. Nasrallah, *Prediction of Transient Heat and Mass Trasnfer in a Closed Metal-Hydride Reactor*, International Journal of Hydrogen Energy, Vol. 29, pp. 195-208, 2004.

24. Suda, S. and N. Kobayashi, *Reaction Kinetics of Metal Hydride Reactors and Their Mixtures*, Journal of Less-Common Metals, Vol. 73, pp. 119-126, 1980.

25. MacDonald, B. D., and A. N. Rowe, *Impacts of External Heat Trasnfer Enhancements on Metal Hydride Storage Tanks*, Journal of Less-Common Metals, Vol. 31, pp. 1721-1731, 2006.

26. Jemni, A., S.B. Nasrallah, and J. Lamloumi, *Experimental and Theoretical Study of a Metal-Hydrogen Reactor*, International Journal of Hydrogen Energy, Vol. 24, pp. 631-644, 1999.

27. Goodel, P. D., and P. S. Rudman, *Hydriding and Dehydyriding Rates of the $LaNi_5 - H$ System*, Journal of Less Common Metals, Vol.89, pp.117-125, 1983.